1 FRONT MATTER
2
3 **Feasibility of keeping Mars warm with nanoparticles**
4
5 Short title: Feasibility of warming Mars with nanoparticles
6
7 **Authors**
8 Samaneh Ansari[1], Edwin S. Kite[2,*], Ramses Ramirez[3], Liam J. Steele[2,4], Hooman Mohseni[1]
9
10 **Affiliations**
11 1. Department of Electrical and Computer Engineering, Northwestern University; Evanston, IL.
12 2. Department of the Geophysical Sciences, University of Chicago; Chicago, IL.
13 3. Department of Physics, University of Central Florida; Orlando, FL.
14 4. European Center for Medium-Range Weather Forecasts; Reading, UK.
15 * Corresponding author, kite@uchicago.edu
16
17 **Abstract**
18 One-third of Mars' surface has shallow-buried H_2O, but it is currently too cold for use by life.
19 Proposals to warm Mars using greenhouse gases require a large mass of ingredients that are rare on
20 Mars' surface. However, we show here that artificial aerosols made from materials that are readily
21 available at Mars—for example, conductive nanorods that are ~9 μm long—could warm Mars
22 $>5\times10^3$ times more effectively than the best gases. Such nanoparticles forward-scatter
23 sunlight and efficiently block upwelling thermal infrared. Similar to the natural dust of Mars, they
24 are swept high into Mars' atmosphere, allowing delivery from the near-surface. For a particle
25 lifetime of 10 years, two climate models indicate that sustained release at 30 liters/sec
26 would globally warm Mars by ≳30 K and start to melt the ice. Therefore, if nanoparticles can be
27 made at scale on (or delivered to) Mars, then the barrier to warming of Mars appears to not be as
28 high as previously thought.
29
30 **Teaser**
31 Warming Mars with artificial aerosols appears to be feasible.
32
33 **MAIN TEXT**
34
35 **Introduction.**
36 Dry river valleys cross Mars's once-habitable surface (1, 2), but today the icy soil is too cold for
37 Earth-derived life (3-5). Streams may have flowed as recently as 600 kyr ago (6), hinting at a
38 planet on the cusp of habitability. Many methods have been proposed to warm Mars' surface by
39 closing the spectral windows, centered around wavelengths (λ) 22 μm and 10 μm, through which
40 the surface is cooled by thermal infrared radiation upwelling to space (7-9). Modern Mars has a
41 thin (~6 mbar) CO_2 atmosphere that provides only ~5 K greenhouse warming via absorption in the
42 15 μm band (10), and Mars apparently lacks enough condensed or mineralized CO_2 to restore a
43 warm climate (11). The spectral windows can be closed using artificial greenhouse gases (e.g.

44 chloroflourocarbons) (8, 12), but this would require volatilizing ~100,000 megatons of fluorine,
45 which is sparse on the Mars surface. An alternative approach is suggested by natural Mars dust
46 aerosol. Mars dust is almost all ultimately sourced from slow comminution (indirect estimate O(3)
47 liters/second, ref. 13) of iron-rich minerals on Mars' surface. Due to its small size (1.5 µm effective
48 radius), Mars dust is lofted to high altitude (altitude of peak dust mass mixing ratio 15-25 km), is
49 always visible in the Mars sky, and is present up to >60 km altitude (14-15). Natural Mars dust
50 aerosol lowers daytime surface temperature (e.g., 16), but this is due to compositional and
51 geometric specifics that can be modified in the case of engineered dust. For example, a nanorod
52 about half as long as the wavelength of upwelling thermal infrared radiation should interact
53 strongly with that radiation (17).
54
55 **Results.**
56 Consider a 9-µm long conductive nanorod (we consider aluminum and iron) with a ~60:1 aspect
57 ratio, not much smaller than commercially available glitter. Finite-difference time domain
58 calculations (Supplementary Methods) show that such nanorods, randomly oriented due to
59 Brownian motion (18), would strongly scatter and absorb upwelling thermal infrared in the spectral
60 windows, and forward-scatter sunlight down to the surface, leading to net warming (Fig. 1,
61 Figs. S1-S4). Results are robust to changing particle material type, cross-sectional shape, and mesh
62 resolution, and change as expected with particle length and aspect ratio (Figs. S5-S8). The
63 calculated thermal infrared scattering is near-isotropic (Fig. 1), which favors surface warming (19).
64 Such nanorods would settle >10× more slowly in the Mars atmosphere than natural Mars dust
65 (Supplementary Methods), implying that once the particles are lifted into the air they would be
66 lofted to high altitude and have a long atmospheric lifetime.
67
68 This motivates calculating surface warming (K) as a function of (artificial) aerosol column density
69 (kg/m^2). The MarsWRF global climate model is suitable for such a calculation (20-22). Following
70 many previous works (22-26), we prescribe a layer of aerosol, and calculate the resulting steady-
71 state warming (Supplementary Methods). Our calculation does not include dynamic transport of
72 aerosol, but includes realistic topography, seasonal forcing, and surface thermophysical properties
73 and albedo. The model output (Fig. 2, Figs. S9-S19) shows that Al nanorod column density
74 160 mg/m^2 yields surface temperatures and pressures permitting extensive summertime (i.e., the
75 warmest ~70 sols period each year) liquid water in locations with shallow ground-ice.
76 This is >5000× more effective, on a warming-per-unit-mass-in-the-atmosphere basis, than the
77 current state of the art (8) (Supplementary Methods). Temperatures experienced by subsurface ice
78 will be lower due to insulation by soil. Water ice at <1 m depth is almost ubiquitous poleward of
79 ±50° latitude (blue lines in Fig. 2) (1). H$_2$O ice is present further equatorward (27), but is insulated
80 beneath >1 m soil cover and so would not melt unless the annual average surface temperature is
81 raised close to 273K.
82
83 The greenhouse effect depends on the temperature difference between the top of the optically thick
84 IR emitting/absorbing layer and that of the planet surface; higher clouds have a bigger ΔT relative
85 to the surface (due to adiabatic cooling) and so give a stronger greenhouse effect. Therefore,
86 the results depend on both artificial-dust-layer-top height and column density (28). Supplementary

87   Table 2 and Fig. S19 show the results varying the layer-top height between ~35 km and ~28 km.
88   The minimum column density for substantial warming (Fig. 2c) can be estimated by setting optical
89   depth in the spectral window (τ_{win}) to unity and solving the following expression for column
90   density M_c (mg/m^2) (e.g. 24):

91    $$\tau_{win} = 3\, Q_{eff}\, M_c\, /\, (4\, r\, \rho) \quad (1)$$

92

93   Here, Q_{eff} is the wavenumber-dependent extinction efficiency, ρ is the nanorod particle density
94   (Al: 2.7 g/cc), and r is the effective nanorod particle radius (the radius of a sphere of equivalent
95   volume, 0.38 μm). Here, Q_{eff} is the ratio of the extinction cross-section in the spectral window
96   (about one-half the maximum cross-section, i.e. 3×10^{-11} m^2, from Fig. 1) to the geometric cross-
97   section of the equivalent sphere, and is $\approx$60. This gives a minimum column density (M_c) of 20
98   mg/m^2. At 160 mg/m^2, the volumetric density of nanorods, 10 cm^{-3}, gives a Brownian coagulation
99   timescale (for 0.1-10 μm diameter spheres, for 100% accretion efficiency) $\approx$ 6 years (18). This
100   timescale estimate has substantial uncertainties; for example, actual accretion efficiency may be
101   less, for example because monodisperse particles of uniform composition (e.g. nanorods) may
102   carry similar charges and thus repel each other (29). On Mars, particles would be taken up by dry
103   deposition and by transient CO_2 ice, and re-released to the atmosphere by dust lifting. Initial release
104   (after manufacture) could be from a pipe extending 10-100m above the surface, as Mars turbulent
105   updrafts strengthen with distance from the surface (30). For an effective particle lifetime of 10
106   years, sustaining the warming shown in Fig. 2a requires particle fountaining at an average rate of
107   30 liters/sec (1 liter/sec corresponds to the flow of one standard garden sprinkler). Multi-year
108   lifetimes are consistent with one-pass fall-out of ~0.1 μm-diameter particles (31), and particle
109   lifetime might be greatly extended if the particles are engineered to self-loft (32-34), further
110   reducing the sustaining mass flux; however, effective particle lifetime remains a major uncertainty
111   in our model.

112

113   As a check on the 3-D results, we ran a 1-D model using annual-average Mars insolation
114   (Supplementary Methods). This predicts 245 K global temperature for ~160 mg/m^2 Al nanorods
115   (Fig. 2c, Figs. S16-S17). For further increases in nanorod loading, the 1-D model predicts lower
116   global temperatures than does the 3-D model. This may be due to differences in the vertical
117   temperature structure of the two models (Supplementary Information).

118

119   Even in the warmed climate, the south pole is cold enough for seasonal CO_2 condensation.

120

121   Within months of warming Mars, the atmospheric pressure increases by ~20% as CO_2 ice
122   sublimes, a positive warming feedback. On a warmed Mars, atmospheric pressure will further
123   increase by a factor of 2-20 as adsorbed CO_2 desorbs (35), and polar CO_2 ice (36) is volatilized on
124   a timescale that could be as long as centuries. This will further increase the area that is suitable for
125   liquid water (6). However, raising Mars' temperature, by itself, is not sufficient to make the planet's
126   surface habitable for oxygenic photosynthetic life: barriers remain (7). For example, Mars' sands
127   have ~300 ppmw nitrates (37), and Mars' air contains very little O_2, as did Earth's air prior to the
128   arrival of cyanobacteria. Remediating perchlorate-rich soil might require bioremediation by
129   perchlorate-reducing bacteria, which yield molecular oxygen as a natural byproduct (38).

130

Discussion.

The results from this relatively simple workflow are subject to several uncertainties that motivate more sophisticated modeling. As one of several examples, modeling of coupled dust flow and ice nucleation on Mars is currently at an early stage (39). Modeling the effect of nanorods as ice nuclei - which could either be a positive or a negative feedback, depending on the size and altitude of the resulting water ice cloud particles and their precipitation efficiency - is additional motivation to study this coupling. A thin coating on the nanorods could alter their hydrophobicity level, and potentially the ice nucleation, and might also protect against oxidation. The optimal location(s) for particle fountaining require further research. Release into the ascending limb of the Hadley cell should allow dispersal in both hemispheres. The radiative effect of water vapor feedback is unambiguously positive. Tests varying nanorod size, composition, and shape suggest that further improvements to warming effectiveness are possible (Figs. S7-S8). For example, extinction efficiency decreases approximately linearly with rod radius, but mass decreases quadratically with rod radius.

With the caveats above in mind, Fig. 2c allows a first estimate of how much surface material would be needed to supply the fountains. For surface-material density 2 g/cc, and Al_2O_3 content of ~10 wt% (e.g., 40), raising the surface temperature to that shown in Fig. 2a over 10 years would require processing 2×10^7 m^3/yr surface material to obtain 7×10^5 m^3/yr of metal, corresponding to a prismatic mine of half-width 350m and side-wall slope 20°, lengthening by 250m per year. This is much easier than the current state-of-the-art (8), because fluorine is only infrequently detected by rovers (41), and is present in most Mars meteorites only at 15-90 ppmw concentrations (42). However, even this reduced material-processing demand still corresponds to 1×10^{-3} of Earth's metal production, and this defines a major manufacturing problem that remains to be solved. Processing of surface material into nanoparticles might use lenses or mirrors to concentrate sunlight for vacuum evaporation, followed by colloidal growth. Synthetic biology (e.g. magnetite nanorods) is a possible alternative (43). Metal 3D printing of parts (e.g. Relativity's Stargate; 44) and/or assembly on Mars might reduce launch costs. Due to their <2 nm width, carbon nanomaterials might warm Mars more effectively than the nanoparticles shown in Figs. 1-2. For example, graphene's density is 0.77 mg/m^2, and graphene nanodisks that are ~10^2 nm diameter have strong mid-infrared resonances (45).

Although nanoparticles could warm Mars (Fig. 2c, Fig. 3), both the benefits and potential costs of this course of action are currently uncertain. For example, in the unlikely event that Mars' soil contains irremediable compounds toxic to all Earth-derived life (this can be tested with Mars Sample Return), then the benefit of warming Mars is nil. On the other hand, if a photosynthetic biosphere can be established on the surface of Mars, perhaps with the aid of synthetic biology, that might increase the Solar System's capacity for human flourishing. On the costs side, if Mars has extant life, then study of that life could have great benefits that warrant robust protections for its habitat. More immediately, further research into nanoparticle design and manufacture coupled with modeling of their interaction with the climate could reduce the expense of this method. Examples include Mars-pressure wind-tunnel experiments for nanorod and dust re-uptake and release rate from realistic rough surfaces (including icy surfaces), and

174 mesoscale/large-eddy-simulation modeling of nanorod dispersal and lofting. In addition to the
175 nanorod warming option and the no-action option, cost-benefit calculations should also consider
176 local-warming methods, such as silica aerogel tiling (9).

178 More work is needed on the very-long-term sustainability of a warmed Mars. Atmospheric escape
179 to space would take at least 300 Myr to deplete the atmosphere at the present-day rate (46).
180 However, if the ground ice observed at meters to tens of meters depth is underlain by empty pore
181 space, then excessive warming over centuries could allow water to drain away, requiring careful
182 management of long-term warming. Subsurface exploration by electromagnetic methods could
183 address this uncertainty regarding how much water remains on Mars deep underground (47).

185 The efficiency of nanoparticle warming suggests that any entity with the goal of strong planet-
186 scale warming would use this approach. This suggests polarization as a technosignature for cold
187 terrestrial worlds with geodynamos.

189 Nanoparticle warming, by itself, is not sufficient to make the planet's surface habitable again.
190 Nevertheless, our study suggests that nanoparticle warming may be of interest to
191 the nanophotonics and planetary science communities, among others, and that further investigation
192 might be fruitful.

194 **Materials and Methods.**
195 *Calculation of optical properties of nanorods.* We carried out finite-difference time domain
196 simulations (FDTD: 3D Electromagnetic Simulator). Optical properties are obtained at
197 75 wavelengths, approximately log-uniformly spaced from 0.24-55 μm (Table S1). Additional
198 details are given in the Supplementary Materials.

200 *Calculation of the surface-warming effect of the nanorods using 1D climate model.* Our single-
201 column radiative-convective climate model (RCM) subdivides atmospheres into multiple vertical
202 log-layers (we implement 201 layers here) that extend from the ground to the top of the atmosphere
203 $(1 \times 10^{-5}$ bar here) (e.g. 25). The RCM has 55 infrared and 38 solar spectral intervals and applies
204 a standard moist convective adjustment. Additional details are given in the Supplementary
205 Materials.

207 *Calculation of the surface-warming effect of the nanorods using 3D climate model.* We use the
208 MarsWRF code (20-22), with a horizontal resolution of 5.625° × 3.75°, corresponding to a grid of
209 64 points in longitude × 48 points in latitude. A 40-layer vertical grid is used. A prescribed natural
210 dust aerosol distribution is imposed, giving an average dust optical depth of 0.20 (peaking at 0.43
211 during southern summer). Additional details are given in the Supplementary Materials.

213 **Author contributions.** ESK conceived research. SA, ESK, RR, LJS, and HM designed research.
214 SA, ESK, and RR carried out research. ESK drafted the manuscript. SA, ESK, RR, LJS, and HM
215 edited the manuscript and contributed to the final manuscript.

217 **Competing interests:** Authors declare that they have no competing interests.

218

219 **Data and materials availability.** All data needed to evaluate the conclusions in the paper are
220 present in the paper and/or the Supplementary Materials. Additional data, for example full 3D
221 climate model output files, are stored at Zenodo (doi:10.5281/zenodo.8352416). FDTD:
222 3D Electromagnetic Simulator is commercial code (Lumerical). The MarsWRF source code can
223 be made available by Aeolis Research pending scientific review and a completed Rules of the
224 Road agreement. Requests for the MarsWRF source code should be submitted to
225 mir@aeolisresearch.com.

226

227 **References.**

228

229 1. Mangold, N., Gupta, S.; Gasnault, O.; Dromart, G.; Tarnas, J. D.; Sholes, S. F.; Horgan, B.;
230 Quantin-Nataf, C.; Brown, A. J.; Le Mouélic, S.; Yingst, R. A.; Bell, J. F.; Beyssac, O.; Bosak, T.;
231 Calef, F.; Ehlmann, B. L.; Farley, K. A.; Grotzinger, J. P.; Hickman-Lewis, K.; Holm-Alwmark,
232 S.; Kah, L. C.; Martinez-Frias, J.; McLennan, S. M.; Maurice, S.; Nuñez, J. I.; Ollila, A. M.; Pilleri,
233 P.; Rice, J. W.; Rice, M.; Simon, J. I.; Shuster, D. L.; Stack, K. M.; Sun, V. Z.; Treiman, A. H.;
234 Weiss, B. P.; Wiens, R. C.; Williams, A. J.; Williams, N. R.; & Williford, K. H., Perseverance
235 rover reveals an ancient delta-lake system and flood deposits at Jezero crater, Mars. *Science* **374**,
236 6568, 711-717 (2021).

237

238 2. Grotzinger, J. P., Sumner, D. Y., Kah, L. C., Stack, K., Gupta, S., Edgar, L., Rubin, D.,
239 Lewis, K., Schieber, J., Mangold, N., Milliken, R., Conrad, P. G., DesMarais, D., Farmer,
240 J., Siebach, K., Calef, F., III, Hurowitz, J., McLennan, S. M., Ming, D., Vaniman, D.,
241 Crisp, J., Vasavada, A., Edgett, K. S., Malin, M., Blake, D., Gellert, R., Mahaffy, P.,
242 Wiens, R. C., Maurice, S., Grant, J. A., Wilson, S., Anderson, R. C., Beegle, L., Arvidson,
243 R., Hallet, B., Sletten, R. S., Rice, M., Bell, J., III, Griffes, J., Ehlmann, B., Anderson, R.
244 B., Bristow, T. F., Dietrich, W. E., Dromart, G., Eigenbrode, J., Fraeman, A., Hardgrove,
245 C., Herkenhoff, K., Jandura, L., Kocurek, G., Lee, S., Leshin, L. A., Leveille, R., Limonadi,
246 D., Maki, J., McCloskey, S., Meyer, M., Minitti, M., Newsom, H., Oehler, D., Okon, A.,
247 Palucis, M., Parker, T., Rowland, S., Schmidt, M., Squyres, S., Steele, A., Stolper, E.,
248 Summons, R., Treiman, A., Williams, R., Yingst, A., and MSL Science Team, A habitable
249 fluvio-lacustrine environment at Yellowknife Bay, Gale Crater, Mars. *Science* **343**, no. 6169
250 (2014): 1242777.

251

252 3. Feldman, W.C., Prettyman, T.H., Maurice, S., Plaut, J.J., Bish, D.L., Vaniman, D.T., Mellon,
253 M.T., Metzger, A.E., Squyres, S.W., Karunatillake, S. and Boynton, W.V., Global distribution of
254 near-surface hydrogen on Mars. *J. Geophys. Res. - Planets* **109**, E9 (2004).

255

256 4. Dundas, C.M., Bramson, A.M., Ojha, L., Wray, J.J., Mellon, M.T., Byrne, S., McEwen, A.S.,
257 Putzig, N.E., Viola, D., Sutton, S. and Clark, E., Exposed subsurface ice sheets in the Martian mid-
258 latitudes. *Science* **359**, 6372 (2018): 199-201.

259

260 5. McKay, C.P. (2014), Requirements and limits for life in the context of exoplanets. *Proc. Natl.*
261 *Acad. Sci. USA* **111**(35), 12628-12633.

262

263 6. Dickson, J.L., Palumbo, A.M., Head, J.W., Kerber, L., Fassett, C.I. and Kreslavsky, M.A..
264 Gullies on Mars could have formed by melting of water ice during periods of high
265 obliquity. *Science* **380**, 6652 (2023), pp.1363-1367.
266

267 7. McKay, C.P., Toon, O.B. and Kasting, J.F., Making Mars habitable. *Nature* **352**, 6335 (1991),
268 489-496.
269

270 8. Marinova, M. M., C. P. McKay, and H. Hashimoto. Radiative-convective model of warming
271 Mars with artificial greenhouse gases. *J. Geophys. Res. - Planets* **110**, no. E3 (2005).
272

273 9. Wordsworth, R., L. Kerber, and C. Cockell. Enabling Martian habitability with silica aerogel
274 via the solid-state greenhouse effect. *Nature Astronomy* **3**, 10 (2019): 898-903.
275

276 10. Haberle, R. M. Estimating the power of Mars' greenhouse effect. *Icarus* **223**, 1 (2013): 619-
277 620.
278

279 11. Jakosky, B. M., and C. S. Edwards. Inventory of CO_2 available for terraforming Mars. *Nature*
280 *Astronomy* **2**(8) (2018): 634-639.
281

282 12. Gerstell, M. F., J. S. Francisco, Y. L. Yung, C. Boxe, and E. T. Aaltonee. Keeping Mars warm
283 with new super greenhouse gases. *Proc. Natl. Acad. Sci. USA* **98**, 5 (2001): 2154-2157.
284

285 13. Kite, E. S., and D. P. Mayer. Mars sedimentary rock erosion rates constrained using crater
286 counts, with applications to organic-matter preservation and to the global dust cycle. *Icarus* **286**
287 (2017): 212-222.
288

289 14. McCleese, D.J., Heavens, N.G., Schofield, J.T., Abdou, W.A., Bandfield, J.L., Calcutt, S.B.,
290 Irwin, P.G.J., Kass, D.M., Kleinböhl, A., Lewis, S.R. and Paige, D.A., Structure and dynamics of
291 the Martian lower and middle atmosphere as observed by the Mars Climate Sounder: Seasonal
292 variations in zonal mean temperature, dust, and water ice aerosols. *J. Geophys. Res. - Planets* **115**,
293 no. E12 (2010).
294

295 15. Kahre, M. A., J. R. Murphy, C. E. Newman, R. J. Wilson, B. A. Cantor, M. T. Lemmon, and
296 M. J. Wolff. The Mars dust cycle. in Haberle, R. (Ed.), 2017, The Atmosphere and Climate of
297 Mars (2017): 295, Cambridge University Press.
298

299 16. Streeter, P.M., S.R. Lewis, M.R. Patel, J.A. Holmes, and D.M. Kass. Surface warming during
300 the 2018/Mars year 34 global dust storm. *Geophys. Res. Lett.* **47**, no. 9 (2020): e2019GL083936.
301

302 17. Van Vleck, J. H., F. Theory of radar reflection from wires or thin metallic strips. *Journal of*
303 *Applied Physics* **18**, no. 3 (1947): 274-294.
304

305 18. Seinfeld, J., & S. Pandis (2016), Atmospheric chemistry and physics, 3rd edn., Wiley.
306

307 19. Forget, F., and R. T. Pierrehumbert. Warming early Mars with carbon dioxide clouds that
308 scatter infrared radiation. *Science* **278**, no. 5341 (1997): 1273-1276.
309

310 20. Richardson, M. I., A. D. Toigo, and C. E. Newman. PlanetWRF: A general purpose, local to
311 global numerical model for planetary atmospheric and climate dynamics. *J. Geophys. Res. -*
312 *Planets* **112** (2007), E09001.
313

314 21. Toigo, A. D., C. Lee, C. E. Newman, and M. I. Richardson. The impact of resolution on
315 the dynamics of the martian global atmosphere: Varying resolution studies with the MarsWRF
316 GCM. *Icarus* **221**, no. 1 (2012): 276-288.
317

318 22. Kite, E. S., L. J. Steele, M. A. Mischna, and M. I. Richardson. Warm early Mars surface
319 enabled by high-altitude water ice clouds. *Proceedings of the National Academy of Sciences* **118**,
320 no. 18 (2021): e2101959118.
321

322 23. Conrath, B.J., Thermal structure of the Martian atmosphere during the dissipation of the dust
323 storm of 1971. *Icarus* **24**(1) (1975), 36-46.
324

325 24. Ramirez, R. M., and J. F. Kasting. Could cirrus clouds have warmed early Mars?, *Icarus* **281**
326 (2017): 248-261.
327

328 25. Ramirez, R.M., 2017. A warmer and wetter solution for early Mars and the challenges with
329 transient warming. *Icarus* **297**, 71-82.
330

331 26. Turbet, M., C. Gillmann, F. Forget, B. Baudin, A. Palumbo, J. Head, and Ö. Karatekin, 2020,
332 The environmental effects of very large bolide impacts on early Mars explored with a hierarchy of
333 numerical models, *Icarus* **335**, 113419.
334

335 27. Dundas, C.M., Mellon, M.T., Conway, S.J., Daubar, I.J., Williams, K.E., Ojha, L., Wray, J.J.,
336 Bramson, A.M., Byrne, S., McEwen, A.S. and Posiolova, L.V., Widespread exposures of extensive
337 clean shallow ice in the midlatitudes of Mars. *J. Geophys. Res. - Planets* **126**, no. 3 (2021):
338 e2020JE006617.
339

340 28. Pierrehumbert, R.T. (2010). Principles of planetary climate. Cambridge University Press.
341

342 29. Fedorova, A. A., F. Montmessin, A. V. Rodin, O. I. Korablev, A. Määttänen, L. Maltagliati,
343 and J-L. Bertaux. Evidence for a bimodal size distribution for the suspended aerosol particles on
344 Mars. *Icarus* **231** (2014): 239-260.
345

346 30. Spiga, A., F. Forget, S. R. Lewis, and D. P. Hinson. Structure and dynamics of the convective
347 boundary layer on Mars as inferred from large-eddy simulations and remote-sensing
348 measurements. *Quarterly Journal of the Royal Meteorological Society* **136**, 647 (2010): 414-428.
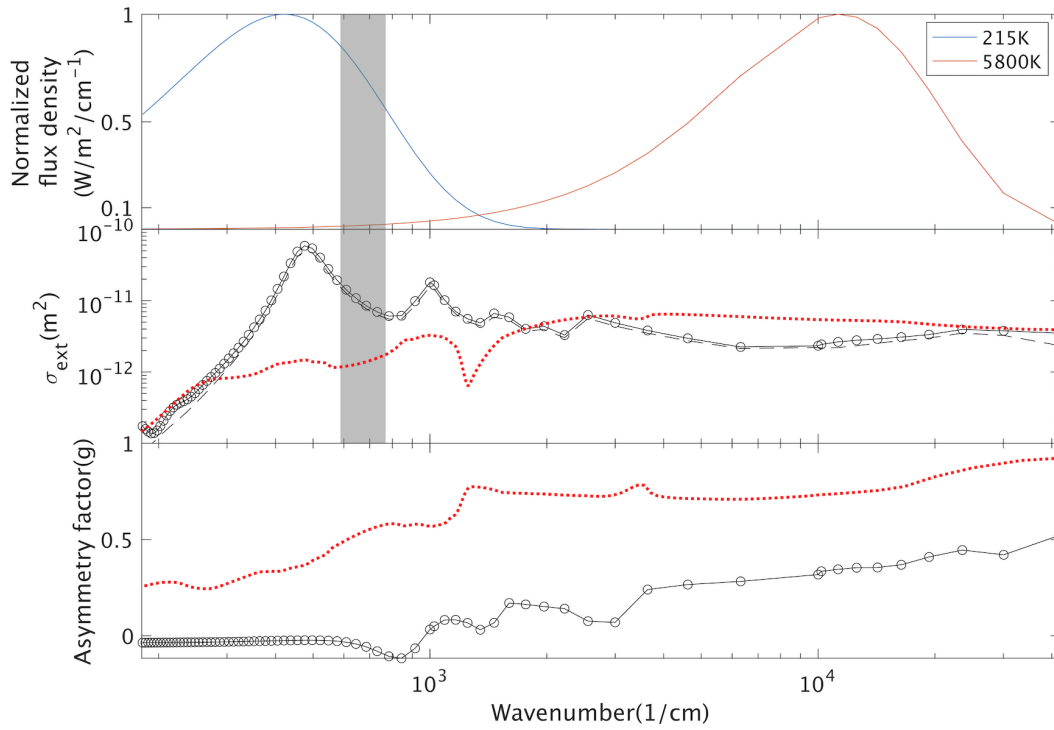349

31. Murphy, J. R., Toon, O. B., Haberle, R. M., & Pollack, J. B. (1990). Numerical simulations of the decay of Martian global dust storms. *Journal of Geophysical Research: Solid Earth*, **95**(B9), 14629-14648.

32. Keith, D. W. Photophoretic levitation of engineered aerosols for geoengineering. *Proc. Natl. Acad. Sci. USA* **107** (2010): 16428-16431.

33. Daerden, F., J. A. Whiteway, L. Neary, L. Komguem, M. T. Lemmon, N. G. Heavens, B. A. Cantor, E. Hébrard, and M. D. Smith. A solar escalator on Mars: Self-lifting of dust layers by radiative heating. *Geophys. Res. Lett.* **42**, no. 18 (2015): 7319-7326.

34. Azadi, M., G. A. Popov, Z. Lu, A. G. Eskenazi, A. Ji Won Bang, M. F. Campbell, H. Hu, and I. Bargatin. Controlled levitation of nanostructured thin films for sun-powered near-space flight. *Science Advances* **7**, no. 7 (2021): eabe1127.

35. Buhler, P. B., and S. Piqueux. Obliquity-Driven CO_2 Exchange Between Mars' Atmosphere, Regolith, and Polar Cap. *J. Geophys. Res. - Planets* **126**, no. 5 (2021): e2020JE006759.

36. Phillips, R.J., Davis, B.J., Tanaka, K.L., Byrne, S., Mellon, M.T., Putzig, N.E., Haberle, R.M., Kahre, M.A., Campbell, B.A., Carter, L.M. and Smith, I.B., 2011. Massive CO_2 ice deposits sequestered in the south polar layered deposits of Mars. *Science* **332**(6031), 838-841.

37. Stern, J. C., Sutter, B., Jackson, W. A., Navarro-González, R., McKay, C. P., Ming, D. W., ... & Mahaffy, P. R. (2017). The nitrate/(per) chlorate relationship on Mars. *Geophysical Research Letters* **44**(6), 2643-2651.

38. Davila, A. F., D. Willson, J. D. Coates, and C. P. McKay. Perchlorate on Mars: a chemical hazard and a resource for humans. *Intl. Journal of Astrobiology* **12** (2013): 321-325.

39. Bertrand, T. R. J. Wilson, M. A. Kahre, R. Urata, and A. Kling. Simulation of the 2018 global dust storm on Mars using the NASA Ames Mars GCM: a multitracer approach. *J. Geophys. Res. - Planets* **125**, no. 7 (2020): e2019JE006122.

40. O'Connell-Cooper, C. D., Spray, J. G., Thompson, L. M., Gellert, R., Berger, J. A., Boyd, N. I., ... & VanBommel, S. J. (2017). APXS-derived chemistry of the Bagnold dune sands: Comparisons with Gale Crater soils and the global Martian average. *Journal of Geophysical Research: Planets* **122**(12), 2623-2643.

41. Forni, O., Gaft, M., Toplis, M. J., Clegg, S. M., Maurice, S., Wiens, R. C., ... & Dyar, M. D. (2015). First detection of fluorine on Mars: Implications for Gale Crater's geochemistry. *Geophysical Research Letters* **42**(4), 1020-1028.

42. Rampe, E.B., Cartwright, J.A., McCubbin, F.M., Osterloo, M.M. (2018). The Role of Halogens During Fluid and Magmatic Processes on Mars. In: Harlov, D., Aranovich, L. (eds) The Role of

Halogens in Terrestrial and Extraterrestrial Geochemical Processes. Springer Geochemistry. Springer, Cham. https://doi.org/10.1007/978-3-319-61667-4_16

43. Lang, C., D. Schüler, and D. Faivre. Synthesis of magnetite nanoparticles for bio- and nanotechnology. *Macromolecular bioscience* **7**, 2 (2007): 144-151.

44. Salmi, B. 3D-printing a rocket. *IEEE Spectrum* **56,** no. 11 (2019): 22-29.

45. Koppens, F. H., Chang, D. E., & García de Abajo, F. J. (2011). Graphene plasmonics: a platform for strong light–matter interactions. *Nano letters* **11**(8), 3370-3377.

46. Jakosky, B.M., Brain, D., Chaffin, M., Curry, S., Deighan, J., Grebowsky, J., Halekas, J., Leblanc, F., Lillis, R., Luhmann, J.G. and Andersson, L., Loss of the Martian atmosphere to space: Present-day loss rates determined from MAVEN observations and integrated loss through time. *Icarus* **315** (2018): 146-157.

47. Grimm, R. E. Low-frequency electromagnetic exploration for groundwater on Mars. *Journal of Geophysical Research: Planets* **107**, no. E2 (2002): 1-1.

48. Wolff, M. J., and R. T. Clancy. Constraints on the size of Martian aerosols from Thermal Emission Spectrometer observations. *J. Geophys. Res. - Planets* **108**, no. E9 (2003).

49. Iwabuchi, H., and P. Yang. Temperature dependence of ice optical constants: Implications for simulating the single-scattering properties of cold ice clouds. *Journal of Quantitative Spectroscopy and Radiative Transfer* **112**, no. 15 (2011): 2520-2525.

50. Querry, M. R. Optical constants. US Army Armament, Munitions & Chemical Command, Chemical Research & Development Center (1985).

51. Rakić, A. D. Algorithm for the determination of intrinsic optical constants of metal films: application to aluminum. *Applied optics* **34**, no. 22 (1995): 4755-4767.

52. Cahill, J., D. T. Blewett, N. V. Nguyen, A. Boosalis, S. J. Lawrence, and B. W. Denevi. Optical constants of iron and nickel metal and an assessment of their relative influences on silicate mixture spectra from the FUV to the NIR. *Icarus* **317** (2019): 229-241.

53. Neubrech, F., and A. Pucci. Plasmonic enhancement of vibrational excitations in the infrared. *IEEE Journal of selected topics in quantum electronics* **19**, no. 3 (2012): 4600809.

54. Novotny, L. Effective wavelength scaling for optical antennas. *Phys. Rev. Lett.* **98**, no. 26 (2007): 266802.

55. Kasting, J., Whitmire, D., and Reynolds, R., Habitable Zones Around Main Sequence Stars, *Icarus* **101** (1993), 108–128.

439 56. Manabe, S. and Wetherald, R.T. (1967), Thermal equilibrium of the atmosphere with a given
440 distribution of relative humidity. *J. Atmospheric Sciences* **24**(3), 241-258.
441
442 57. Thekaekara, M.P. (1973), Solar energy outside the earth's atmosphere. *Solar energy* **14**(2),
443 109-127.
444
445 58. Ramirez, R. M., Kopparapu, R., Zugger, M. E., Robinson, T. D., Freedman, R., & Kasting, J.
446 F. (2014). Warming early Mars with CO_2 and H_2. *Nature Geoscience*, **7**(1), 59-63.
447
448 59. Mischna, M. A., Lee, C., & Richardson, M. (2012). Development of a fast, accurate radiative
449 transfer model for the Martian atmosphere, past and present. *Journal of Geophysical Research:*
450 *Planets*, **117**(E10).
451
452 60. Millour, E., F. Forget, F. González-Galindo, A. Spiga, S. Lebonnois, S. R. Lewis, L.
453 Montabone., The Mars climate database (version 4.3). No. 2009-01-2395. SAE Technical Paper,
454 2009.
455
456 61. Guzewich, S. D., Talaat, E. R., Toigo, A. D., Waugh, D. W., & McConnochie, T. H. (2013).
457 High-altitude dust layers on Mars: Observations with the Thermal Emission Spectrometer. *Journal*
458 *of Geophysical Research: Planets*, **118**(6), 1177-1194.
459
460 62. Guzewich, S. D., Toigo, A. D., Richardson, M. I., Newman, C. E., Talaat, E. R., Waugh, D.
461 W., & McConnochie, T. H. (2013). The impact of a realistic vertical dust distribution on the
462 simulation of the Martian General Circulation. *Journal of Geophysical Research: Planets*, **118**(5),
463 980-993.
464
465 63. Fonseca, R. M., M.-P. Zorzano-Mier, and J. Martín-Torres. Planetary boundary layer and
466 circulation dynamics at Gale Crater, Mars. *Icarus* **302** (2018): 537-559.
467

476

477
478
479 **Fig. 1. Orientation-averaged optical properties of a 9 µm-long Al nanorod with cross-section**
480 **0.16 µm × 0.16 µm, calculated using a 3D Finite-Difference Time-Domain (FDTD) approach.**
481 Top panel: Planck functions (normalized flux density, W/m²/µm) for 215 K (Mars thermal
482 emission now, red) and 6000 K (insolation, blue). For context, the CO_2 band is overlain (gray
483 shading) at 12-16 µm. Middle panel: Solid black line corresponds to total extinction, dotted black
484 line to scattering. Lower panel shows scattering asymmetry. Also shown are wavelength
485 dependence of total extinction and asymmetry factor for natural dust assuming a log-gaussian
486 particle size distribution centered on 2.5 µm (48) (red dotted lines).
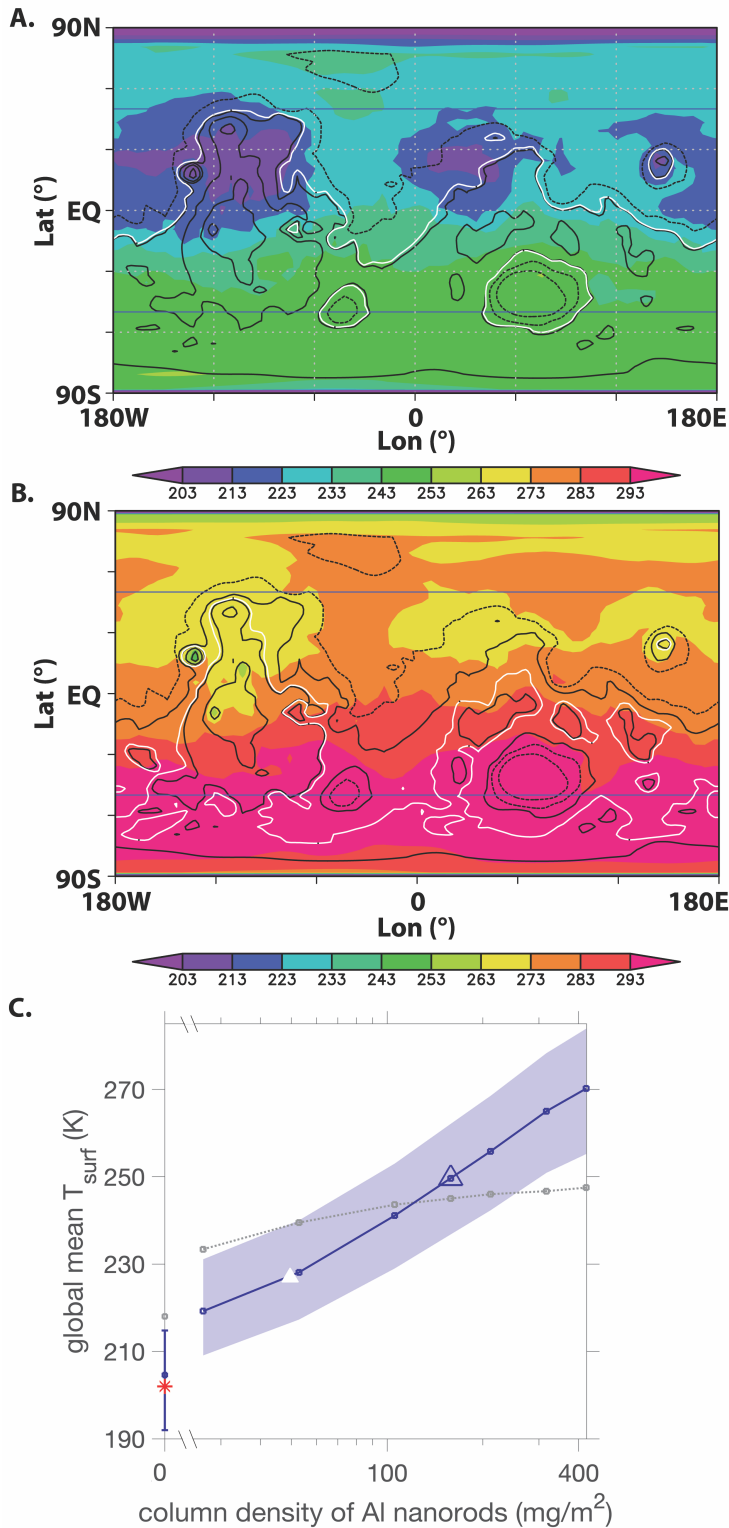
Fig. 2. 3D model output. Warm-season temperatures (K) (color shading) on (A) Mars with addition of ~160 mg/m² of Al nanorods, (B) control case. This corresponds to the average surface temperature during the warmest 36° of solar longitude (~70 days) of the year. White contour corresponds to 610 Pa (~6 mbar) mean pressure level. Black contours correspond to topographic elevation in m (dashed: -5 km and –2 km, solid: 0 km, +2km, and +5 km). Blue lines: approximate latitudinal (equatorward) extent of ice at <1 m depths. Results do not include CO_2 outgassing from within polar ice, which would cause further warming. (C) Dependence of planet-averaged surface warming on Al-nanorod column mass. The blue envelope corresponds to the modeled seasonal range in global mean T_{surf}. Gray corresponds to 1-D results (see text for details). Blue line corresponds to 3-D results. Blue triangle corresponds to panel (a), and white triangle marks onset of warm-season temperatures above the freezing point of water at 50°S. Symbols on y-axis are temperatures for the no-nanorod case, with the red asterisk corresponding to observed Mars value. Additional details including comparison to Fe nanorods are shown in Figs. S10-S19.
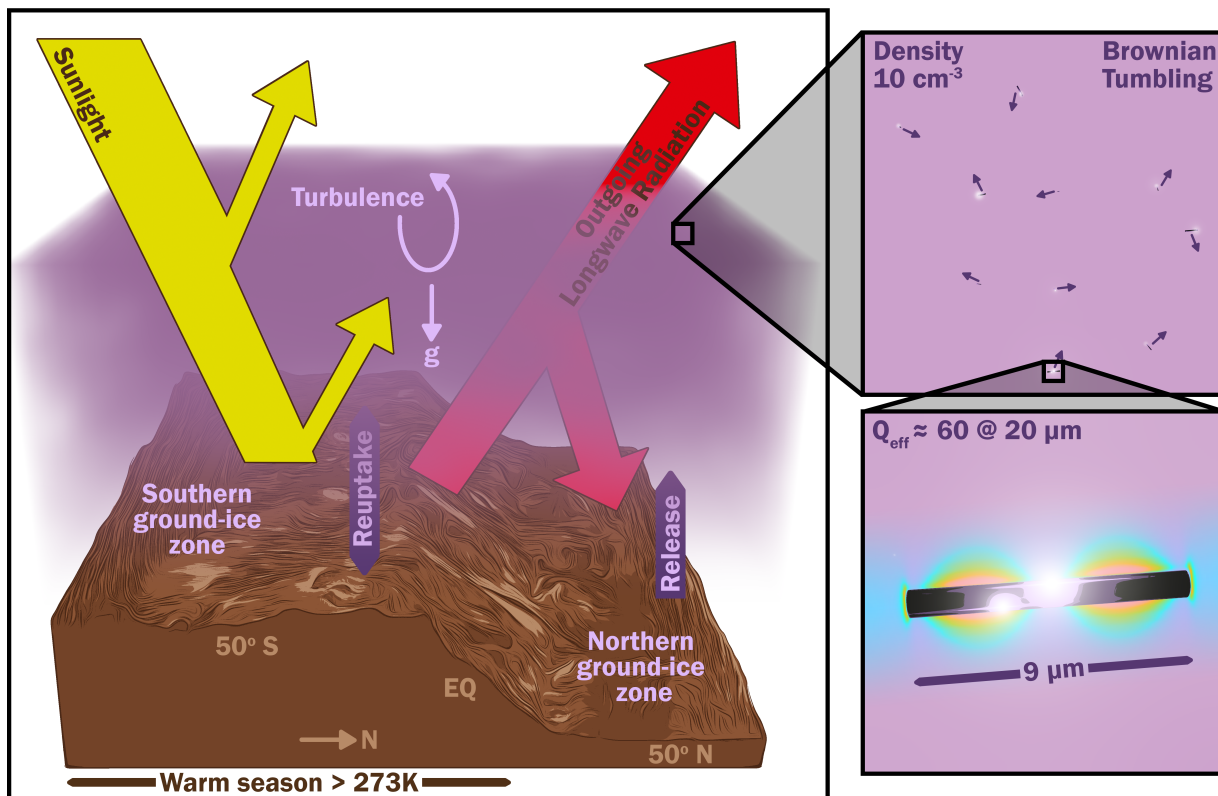
Fig. 3. Graphical summary. This figure shows a graphical summary of the proposed warming method. Figure credit: Aaron M. Geller, Northwestern, CIERA + IT-RCDS.

Supplementary Materials for

Feasibility of keeping Mars warm with nanoparticles

Samaneh Ansari *et al.*

*Corresponding author: Edwin S. Kite. Email: kite@uchicago.edu

This PDF file includes:

Supplementary Text.

1. Calculation of optical properties of nanorods.

Simple calculations (e.g., ref. 17) suggest that 9 μm long conductive nanorods with a 60:1 aspect ratio would have a strong and broad extinction in the ~22 μm spectral window. To test this, we carried out finite-difference time domain simulations (FDTD: 3D Electromagnetic Simulator). First, we verified that the FDTD simulations reproduce Mie theory for water ice spheres (49) (Fig. S1). The nanorod FDTD simulations use a pulse of light whose interaction with the simulated nanoparticle is Fourier-decomposed to obtain the λ-dependence of the absorption and scattering cross sections as well as the scattering asymmetry. The representation of the angular distribution of scattered light by a single parameter, the scattering asymmetry, is standard in climate modeling (e.g., 28). 75 wavelengths, approximately log-uniformly spaced from 0.24-55 μm, are obtained (Table S1). We used refractive indices for Fe from Ref. 50, and for Al from Ref. 51. Ref. 52 suggest that Fe refractive indices obtained prior to their own work might be affected by Fe-oxidation, but as Mars' atmosphere is ~0.1% O_2 some degree of oxidation is inevitable, so this is acceptable. Implementation involved combining three different simulations for different λ ranges, for computational feasibility. 75 simulations were carried out for the 9 μm long nanorod, corresponding to the product of 5 orientations in θ, 5 orientations in φ (0°, 30°, 45°, 60°, and 90°, for both angles), and three λ ranges. Here, θ corresponds to rotations in the E-H plane and the other rotation is termed φ (k-E plane, symmetric and similar to k-H plane) (Fig. S2). Far-field methods were employed to obtain the scattering phase function. We anticipate that actual nanorods will have circular cross-sections. Because of computational limitations associated with the FDTD approach, we model a nanorod with square cross-section, but find that switching between circular and square cross-sections makes negligible difference to the calculated optical properties (Fig. S3).

As expected, the simulated nanorods showed strong, broad absorptions near 22 μm (Fig. 1), supporting their suitability for Mars warming. This is consistent with previous work on Ag nanorods (53). The wavelength of the absorption peak is slightly longer than double the rod length, due to plasma effects (54). In order to average over orientations (Fig. S4), rod orientation was uniformly sampled on the sphere relative to the incident electric field vector (~1000 samples between 0° and 90° for both angles) and optical properties interpolated using a spline in the grid of 25 computed orientations for each λ. The orientations of nanorods in the atmosphere are assumed to be random and uniform, hence averaging over a spherically equidistant grid of orientations would result in proper orientation-averaged characteristics. We found (minor) infrared back-scattering in these simulations. A sensitivity test using the 3D model for Fe nanorods showed that this choice makes little difference (~0.3 K) to the calculated temperatures.

To check the interpolation accuracy, we did check runs on multiple intermediate points (Fig. S5). When the rod is viewed nearly end-on, the interpolation results grow less accurate. However, end-on geometries are infrequently encountered, and at the higher angles, the scattering and absorption cross-sections are substantially smaller, so the effect of these points on the overall orientation average is insignificant. To check the simulation accuracy, we did a check run increasing the

552 resolution across the width of the nanorod from 8 simulation mesh points (20 nm spacing) to 10
553 simulation mesh points (16 nm spacing), finding negligible differences (Fig. S6).
554
555 We also did calculations for 7.5 μm-long Fe nanorods with cross-section 0.08 μm × 0.08 μm,
556 finding peak extinction around 20 μm (Fig. S7), and less climate warming per nanorod, but more
557 climate warming per kg of nanorods. An optimal warming approach might use a mix of rods of
558 different lengths. Moreover, we find that the total extinction (absorption plus scattering) for Al
559 nanorods is the same as for Fe nanorods (Fig. S8), and the corresponding warming is also about
560 the same (Table S2), even though the density of Al is three times less than that of Fe. Fe, Al, and
561 Mg are all present at >4 wt% level in Mars soil. We focus here on Al and Fe because optical
562 properties are available over the full wavelength range of interest (other metals are worthy of future
563 investigation). This suggests that further research might yield further improvements in the
564 effectiveness of warming.
565
566 2. Calculation of the surface-warming effect of the nanorods using 1D climate model.
567 Our single-column radiative-convective climate model (RCM) subdivides atmospheres into
568 multiple vertical log-layers (we implement 201 layers here) that extend from the ground to the top
569 of the atmosphere (1×10^{-5} bar here) (e.g. 25). The RCM has 55 infrared and 38 solar spectral
570 intervals (55). The model applies a standard moist convective adjustment (e.g. 56). Should
571 tropospheric radiative lapse rates exceed their moist adiabatic values, the model relaxes to a moist
572 H_2O adiabat at high temperatures or to a moist CO_2 adiabat when temperatures are low enough for
573 CO_2 to condense. The RCM implements a standard solar spectrum (57). For present Mars (solar
574 flux = 585 W/m^2), we assume a typical stratospheric temperature of 155 K and a surface albedo of
575 0.22 (e.g. 24). The atmospheric pressure is a Mars-like 650 Pa with an assumed acceleration due
576 to gravity of 3.73 m/s^2. Although we prescribe a tropospheric relative humidity of 50%, our results
577 are insensitive to this parameter. The baseline mean surface temperature of the resultant pure CO_2
578 atmosphere (without nanorods) is 218 K. For comparison, Mars' observed global mean surface
579 temperature is 202 K (10). The 1D model runs warmer in the 6 mbar no-nanorods case mainly
580 because it lacks day-night and equator-pole temperature contrast, and because it lacks clouds, dust
581 and topography (10). With an assumed surface albedo of 0.22 and solar flux of 585 W/m^2, the
582 predicted equilibrium temperature (T_{eq}) would be ~212 K (assuming a perfect blackbody). This
583 212 K T_{eq} value is the minimum surface temperature for a 1D model with no greenhouse effect.
584 However, our 1D model predicts 6 K greenhouse effect (consistent with data and with other
585 models), raising the mean surface temperature to ~218 K (e.g. 58). In summary, the warm 1D
586 model output gives a useful benchmark comparison on the importance of 3D factors like dust,
587 clouds and topography on modeling predictions in comparison with that from the nanorods.
588
589 One of the reasons for the differences in temperature response between the models is the baseline
590 surface temperature, which is higher in the 1D model (for reasons explained above). The main
591 cause, however, is differences in the vertical temperature profiles across models (e.g., Fig. S18).
592 For instance, lapse rates differ slightly (the top of the cloud deck is at a slightly higher pressure
593 level, or closer to the ground, in the 3D model) and the 3D model has a near-surface temperature
594 inversion which is absent in the 1D code (Fig. S18). The 3D model also has a larger effective

convective region. Tests confirm that the 1D and 3D results agree more closely when the 3D profile is imposed on the 1D model. For example, at $\tau_{Fe} = 0.25$, imposing the same mean surface temperature in the 1D model as is obtained for the 3D model (~225.5 K) yields a top-of atmosphere (TOA) net outgoing longwave radiation/net incident stellar flux ratio of ~0.69 (a value equal to 1 corresponds to a TOA radiative equilibrium). In other words, the 1D model "wants" to warm. However, when the 3D model vertical temperature profile was applied instead (at the same surface temperature), this ratio had increased to 0.86 (removing ~60% of the difference from 1). In other words, most of the difference between the 3D model and the 1D model can be explained by differences in the vertical thermal profile. This suggests that even across 3D models, differences in convective schemes (and temperature profiles) could produce some spread in the results, motivating investigation of engineered warming of Mars using different 3D schemes. Despite these numerical differences, the atmospheric response to nanorod addition in both the 1D and 3D models is qualitatively very similar. In both cases, nanoparticle warming provides a greenhouse effect >5,000× greater than the current state of the art.

Following Refs. 24-25, we calculate the wavenumber-dependent optical depths (τ) for the nanorods from the following expression:

$$\tau = 3\,Q_{eff}\,NRC\,\Delta z\,/\,(4\,r\,\rho) \quad (2)$$

Here, *NRC* is the nanorod content (g/m^3) and Δz is the path length. This equation differs from (1) only in that the optical depth is integrated over all nanorod heights and across all wavenumbers, not just in the spectral window. The nanorods are well-mixed throughout the atmosphere (up to 35 km) above the imposed 500 Pa nanorod-layer base and so *NRC* was assumed to scale linearly with the local pressure. We computed the radius of the sphere with the equivalent nanorod volume, which yields an effective nanorod particle radius of ~0.38 μm for the 9 μm nanorods.

Within the 1D model framework, we implement a simple procedure to calculate nanorod warming. For each assumed nanorod optical depth, we find the surface temperature that yields stratospheric energy balance (i.e. the net outgoing and net incoming fluxes must balance each other) (Figs. S16-S17).

3. Calculation of the surface-warming effect of the nanorods using 3D climate model.

The FDTD output is interpolated to 2000 log-uniformly spaced λ's. We set optical properties at λ >55 μm equal to those at 55 μm (Fig. S9). This approximation is acceptable, because extinction (W/m^2/μm) is minor at such long λ. MarsWRF uses a two-stream radiation code (e.g. 22, 59). Radiative transfer calculations include both gas (for this work, CO_2) and aerosol (for this work, natural dust, nanorods, and CO_2 ice) radiative effects. This implementation of MarsWRF uses Planck-weighted averaging to bin down high-spectral-resolution optical properties. The blackbody temperature used for the Planck-weighted averaging is 6000 K for solar bands (6 bins from 0.24-4.5 μm, with bin edges at 0.24, 0.40, 0.8, 1.31, 1.86, 2.48, 3.24, and 4.5 μm), and 215 K for the thermal infrared bands (6 bins from 4.5-1000 μm, with bin edges at 4.5, 8.0, 12.0, 14.1, 16.0, 24.0,

60, and 1000 μm) (Fig. S9). Thermal equilibrium between gas and dust is assumed. We neglect radiation pressure, magnetic effects, quantum size effects, and temperature dependence of the optical constants.

In the fixed-cloud runs, present-day Mars values are used for orbital parameters, surface albedo, and surface thermal inertia. Mars' southern summer solstice occurs near perihelion, so (by Kepler's second law) northern summer is long and relatively cool, and southern summer is short and warm relative to annual average (Figs. S10-S12). Water vapor abundance in the atmosphere is fixed to zero, which is conservative in that water vapor radiative feedback would increase warming. A prescribed natural dust aerosol distribution is imposed corresponding to the Mars Climate Database MGS-dust-scenario (60), giving an average dust optical depth of 0.20 (peaking at 0.43 during southern summer). Natural dust aerosol warms the atmosphere but lowers daytime surface temperature. The artificial-aerosol layer is parameterized by a layer-base pressure (in Pa), a layer vertical thickness (in units of model levels), and the nanorod orientation-averaged optical depth at a reference λ (0.67 μm). Because the model levels are specified in η coordinates (where $\eta = P/P_{surf}$, where the model-top pressure has been subtracted from both pressures), the aerosol layer is physically more compact over the poles because low temperatures compact the air column. We refer to the altitude away from the poles below which 95% of the particles are contained as the "aerosol layer top height". The nanorod mixing ratio is assumed to be uniform within the nanorod layer (Fig. S13). We prescribe a layer-base level of 500 Pa and vary the layer thickness. This approach gives a maximum in artificial-aerosol opacity above the surface, which is also observed for natural Mars dust aerosol (61-62). Buffering by latent heat implies that melting either ice cap to form seas would take at least centuries.

Settling for a 0.1 μm-radius dust particle for 1 scale height at Mars surface pressure takes 3 years (Murphy 1990). Extrapolation to Al nanorods with radius 0.04-0.08 μm suggests settling times that are similar or greater. Increase of Mars' atmospheric pCO_2 under warming will decrease the Knudsen number and hinder dust settling. One-pass settling rates are much slower than that of natural Mars dust, and effective particle lifetime will be longer due to re-entrainment.

The runs presented here use a horizontal resolution of 5.625° × 3.75°, corresponding to a grid of 64 points in longitude × 48 points in latitude. A 40-layer vertical grid is used, using a modified-η (terrain-following) coordinate ($\eta = P/P_{surf}$, where the model-top pressure has been subtracted from both pressures). The dynamical timestep varies between runs but is never longer than 1-min. The planetary boundary layer scheme is based on that in Ref. 63, and the surface layer uses a Monin-Obukhov scheme. Runs are initialized from a cold state and continue until the simulated annual seasonal cycle is highly repeatable from year to year. We found that runs require only a single year of spin-up adjustment, as modern Mars, lacking seas, has low effective thermal inertia. Output is reported from the third year of each model run. Mean wind speed ~30 m above the surface increases from 8 m/s in the no-nanorods case to 13 m/s in the Fig. 2a (with-nanorods) case, which would stir up more dust (and nanorods). Daytime near-surface turbulence on Mars is sufficient to loft dust (and therefore nanorods) released at 10-100m altitude at all latitudes for P > 6 mbar. Sensitivity tests adjusting model resolution, and varying nanorod distribution and other parameters are listed in Table S3.

683 For the no-nanorods case (Fig. 2b), the global and annual average shortwave radiation reaching
684 the surface is 133.1 W/m^2 (119.7 W/m^2 direct beam and the remainder diffuse/scattered), of which
685 104.2 W/m^2 is absorbed with the rest being reflected. The spatially- and time-averaged surface
686 albedo, including ice, is 0.237. The global/annual average longwave radiation at the surface
687 (greenhouse effect) is 23.9 W/m^2. The global/annual average longwave emission from the surface
688 is 125.4 W/m^2. The mismatch of -2.7 W/m^2 is caused by limited output sampling, fluxes into the
689 surface (e.g. CO_2 condensation, conduction), and model imprecision. For the with-nanorods case
690 shown in Fig. 2a, the global and annual average shortwave radiation reaching the surface is
691 89.2 W/m^2 (41.4 W/m^2 direct beam), of which 70.6 W/m^2 is absorbed with the rest being reflected.
692 The spatially- and time-averaged surface albedo, including ice, is 0.208. A greater fraction of
693 sunlight is absorbed due to reduction in reflective seasonal CO_2 ice. The global/annual average
694 longwave radiation at the surface (greenhouse effect) is 186.2 W/m^2. The global/annual average
695 longwave emission from the surface is 254.3 W/m^2. The mismatch of -2.5 W/m^2 (i.e., surface
696 temperature under-stated relative to radiative fluxes) is caused by limited output sampling, fluxes
697 into the surface (e.g. CO_2 condensation, conduction), and model imprecision.

699 The runs shown in Fig. 2c correspond to optical depths at $\lambda = 0.67$ µm of {0, 0.125, 0.25, 0.5, 0.75,
700 1, 1.5, 2}. Details for selected values are given in Fig. S14. The conversion factor is 545 mg/m^2
701 for Fe and 212 mg/m^2 for Al for one optical depth. Optical depths in the spectral windows are
702 much greater than at 0.67 µm (Fig. 1). Output was sampled at 260 equally spaced intervals per
703 Mars year. This provides (deliberately aliased) sampling of the day-night cycle during each season
704 at each longitude and latitude. A sensitivity test using 1300 output steps showed negligible (≤0.1
705 K) differences in both annual-average and seasonal warming (Table S3). Mars' atmosphere is thin,
706 with low thermal inertia and limited ability to transport heat laterally, and the tests with artificial
707 imposed patchy or unsteady nanorod distribution show that the corresponding warming is sharply
708 confined in space and time. This suggests that it might be possible to enhance warming at preferred
709 latitudes and seasons. The atmosphere and surface temperature quickly responds to the radiative
710 forcing at the release site/time, and after injection ceases, spreading of the particles away from the
711 release site ensures that the warming at the release site soon decreases.

713 <u>4. Possible hazards.</u>

715 Natural Mars air is unsafe for humans to breathe because it has almost no oxygen (insufficient for
716 deflagration) and also has a high natural concentration of PM 2.5 (Mars mineral aerosol dust). The
717 nanorod density is ~10 $\mu g/m^3$, which would not substantially alter this situation. A more immediate
718 concern is asbestosis, as humans would bring both natural dust and nanoparticles into settlements
719 via airlocks. One way to mitigate this hazard would be to make nanorods that dissolve or fragment
720 in liquid water.

722 <u>5. Comparison to previous work.</u>

724 To our knowledge, the most effective (on a per-unit-mass-in-the-atmosphere basis) Mars warming
725 agent that has been previously been proposed is the "optimal [gas] mix" of ref. 8, which is mostly

726   C_3F_8 (molecular mass 188 Da). This gives 37.5 K warming for 1 Pa, which corresponds to 170
727     $kg/m^2 \times$ (1 Pa / 650 Pa) $\times$ (~188 Da / 44 Da) $\approx 1.1\ kg/m^2$. This warming is about the same as the
728   nanorod case shown in Fig. 2a, which corresponds to ~160 mg/m^2 of Al nanorods. Therefore this
729   nanorod loading (using non-optimized nanoparticles) is >5000× more effective than the optimal
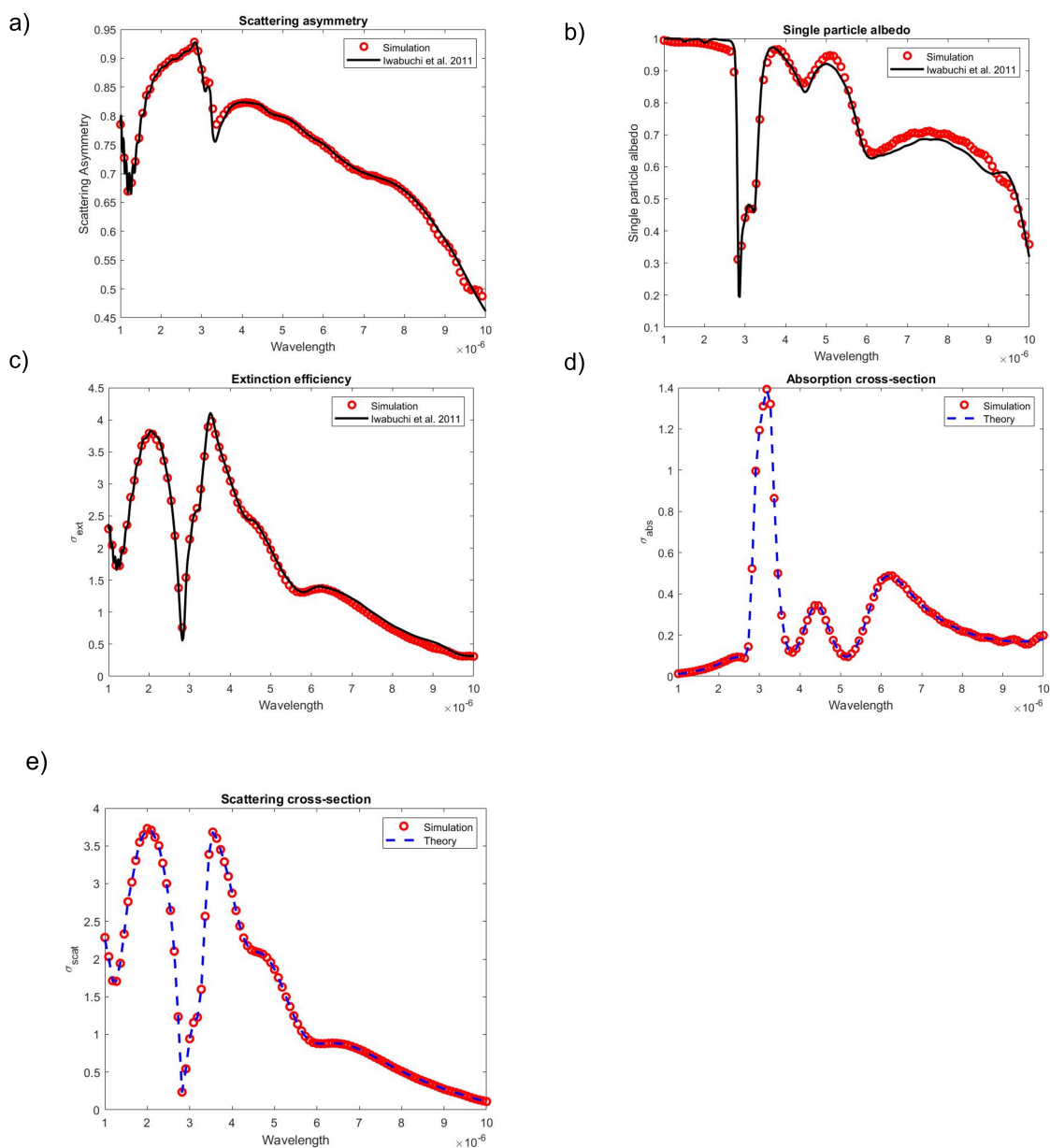730   gas mix.

Fig. S1. (a,b,c) Verification of calculations by comparison to Mie-theory results for a water-ice sphere (49), showing single particle albedo, scattering asymmetry, and extinction efficiency. (d,e) Shows the comparison of analytical Mie scattering results for an ice sphere with simulation outputs.
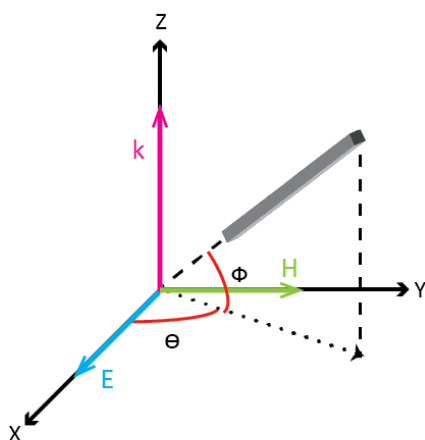
Fig. S2. Illustration showing the definition of the angles θ and φ in the FDTD calculation. "k" corresponds to the direction of the propagation of the incident electromagnetic wave. The gray bar corresponds to the nanorod.

733

734
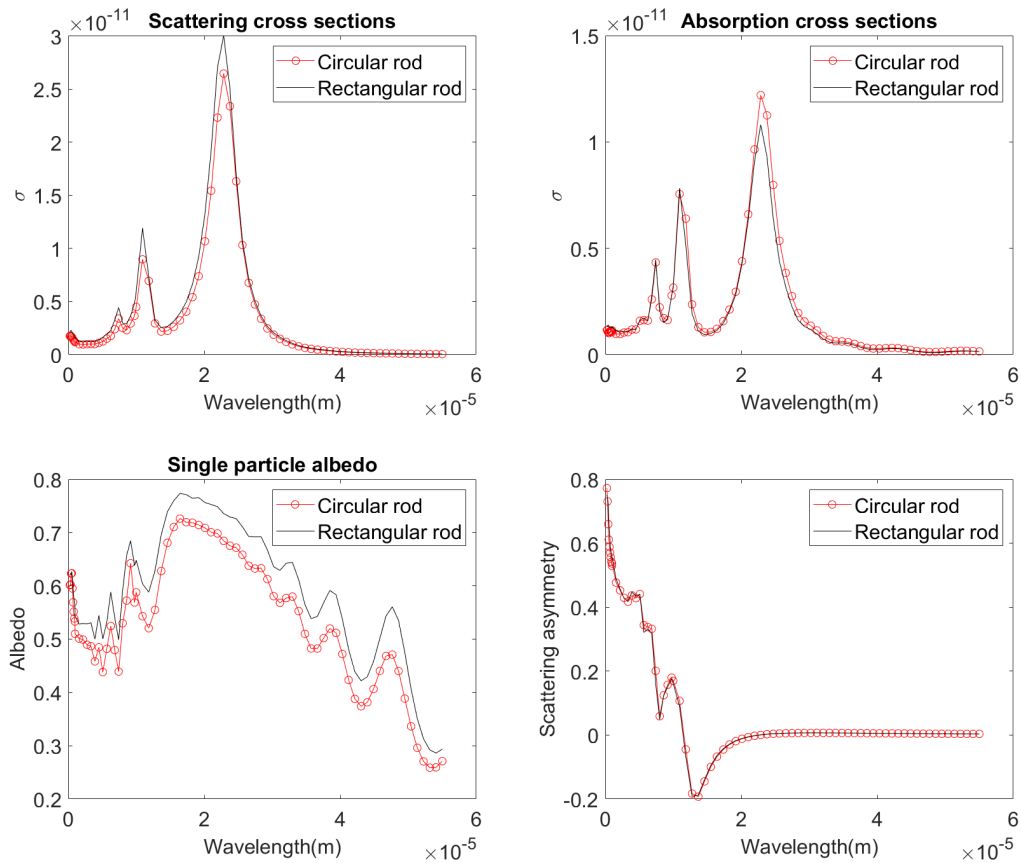
Fig. S3. Switching between a square and circular cross-section for the nanorod has only minor effects on the calculated optical properties. Fe nanorod, 9 µm-long, ~60:1 aspect ratio, orientation: $\theta = 45°$, $\varphi = 45°$.

735
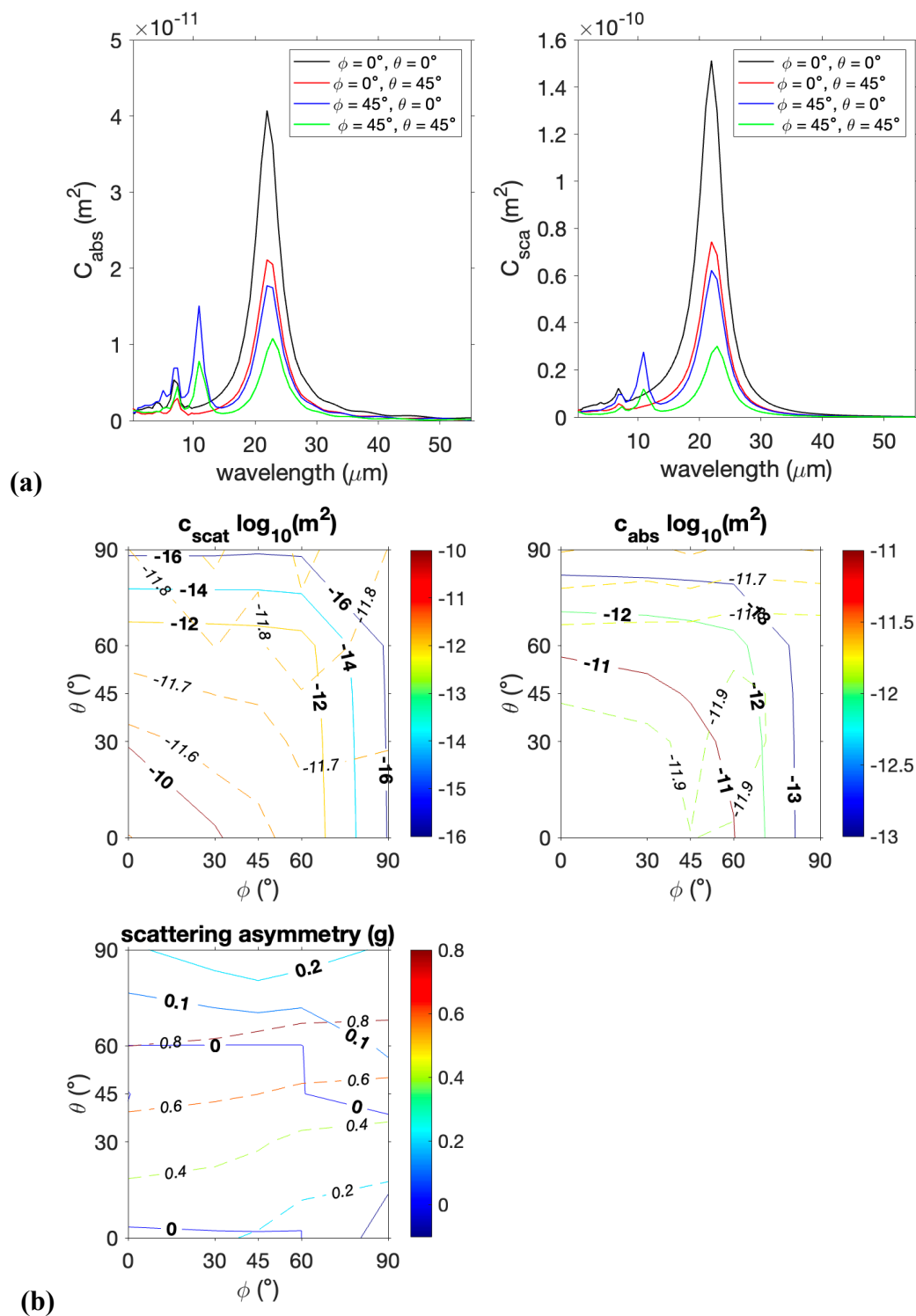
Fig. S4. FDTD output figure, showing orientation dependence of the optical properties of a 9 μm-long, ~60:1 aspect ratio Fe nanorod. (a) Cross-sections as a function of wavelength. (b) Cross-sections and scattering asymmetry as a function of orientation for wavelengths 21.9 μm (solid lines, bold labels) and 0.70 μm (dashed lines, italic labels).

Results of interpolation and simulation at ϕ=15,θ=15
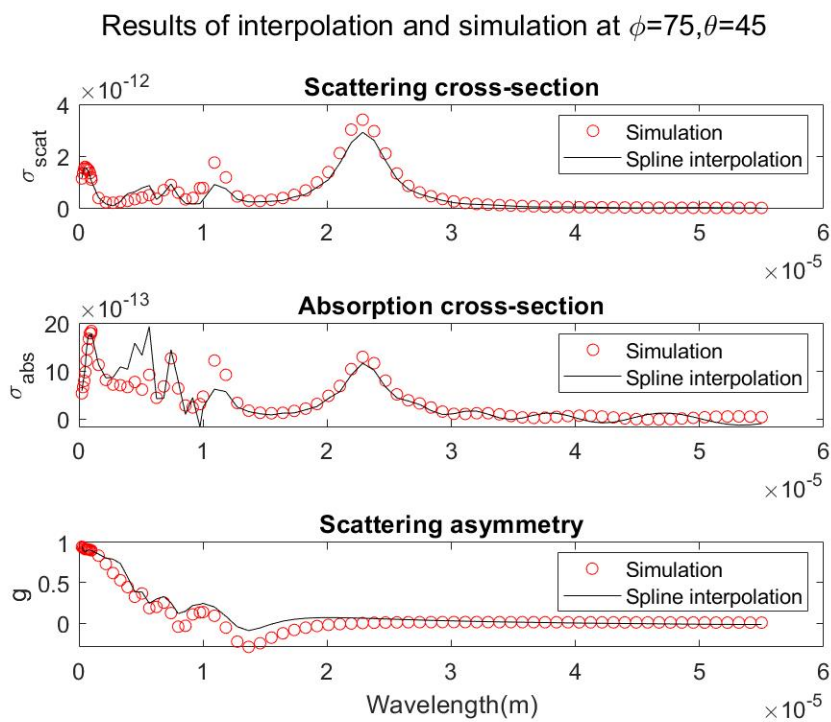

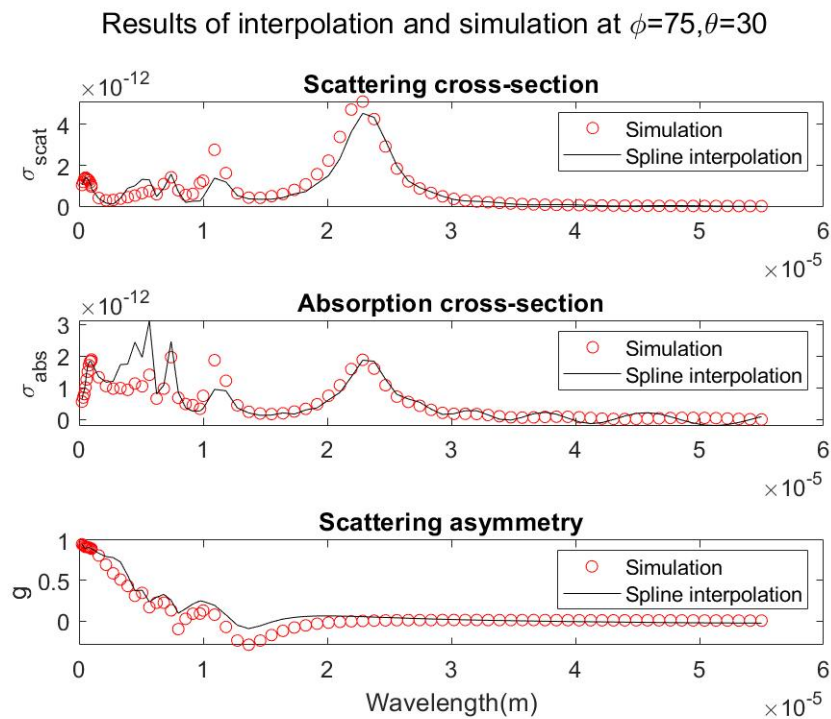Results of interpolation and simulation at ϕ=60,θ=15

Results of interpolation and simulation at ϕ=75,θ=30

Scattering cross-section

Absorption cross-section

Scattering asymmetry

Results of interpolation and simulation at ϕ=75,θ=45

Scattering cross-section

Absorption cross-section

Scattering asymmetry
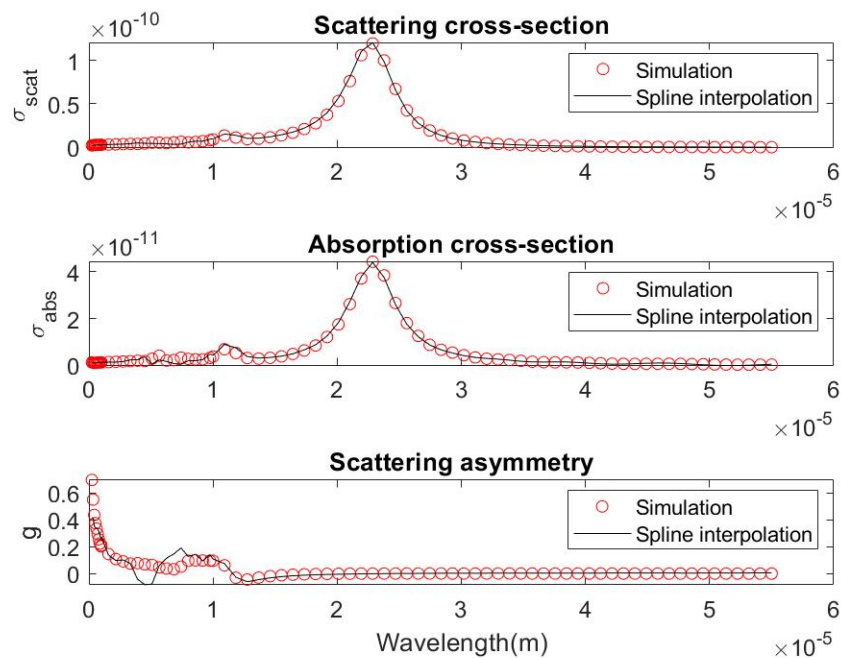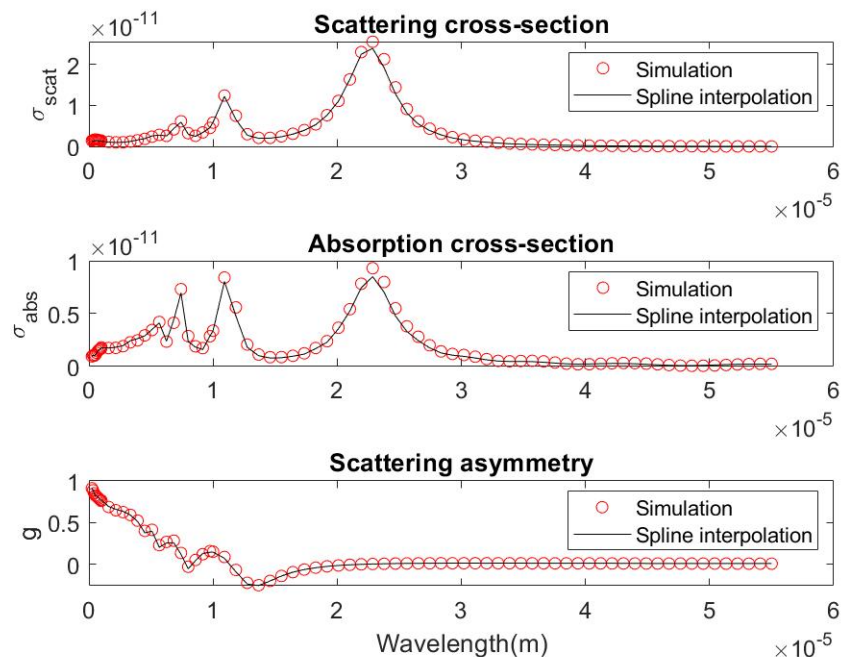
Fig. S5. Results of interpolation check. 9 μm-long, ~60:1 aspect ratio Fe nanorod. Units of angles are degrees.

738

27
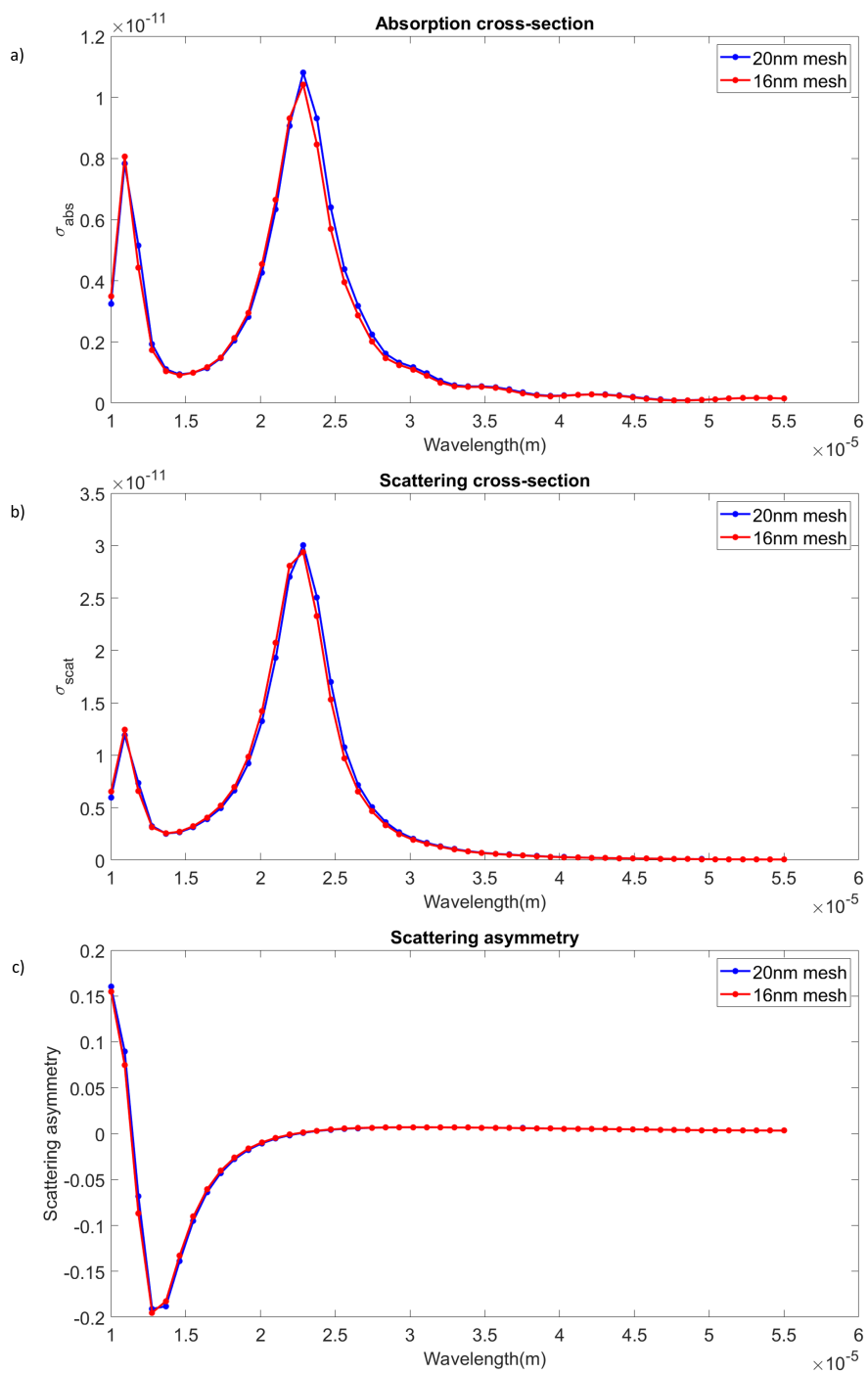
Fig. S6. Sensitivity test showing change in optical properties when mesh resolution is increased (decreasing mesh spacing). 9 µm-long, ~60:1 aspect ratio Fe nanorod. Orientation: θ = 45°, φ = 45°.
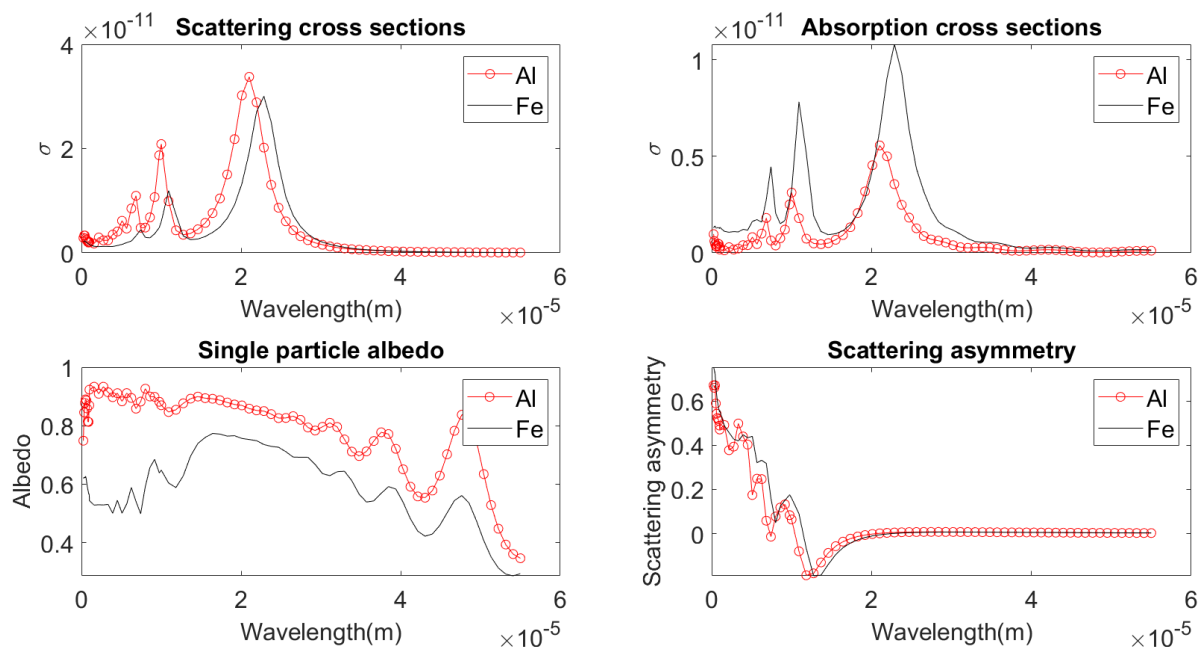
739

Fig. S7. Showing sensitivity of calculated optical properties to changing nanorod composition (Al vs. Fe), for a 9 μm-long, ~60:1 aspect ratio nanorod. The total extinction cross section (scattering plus absorption) and the location of the resonances remains about the same; a small increase in Al nanorod length would be sufficient to closely match the Fe cross-sections. As Al is 3× less dense than Fe, this suggests Al is more effective on a warming-per-unit-mass basis. Conductive-nanorod size and shape, and not composition, are the main controls on simulated nanorod optical properties. Aluminum material properties are obtained from ref. 51. Orientation: θ = 45°, φ = 45°.
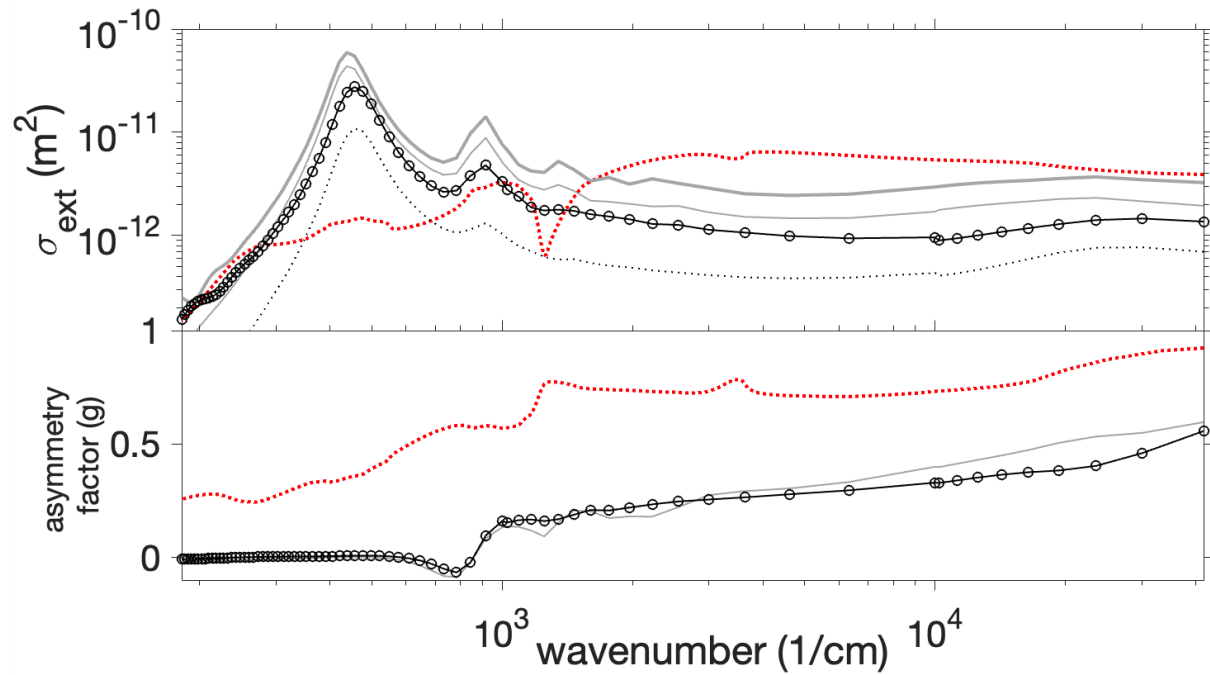
740

741

Fig. S8. Showing the calculated optical properties varying particle length and width for the same particle composition: specifically, 7.5 µm-long Fe nanorods with cross-section 0.08 µm × 0.08 µm, compared to 9 µm-long Fe nanorods with cross-section 0.16 µm × 0.16 µm. Orientation-averaged optical properties calculated using a 3D Finite-Difference Time-Domain (FDTD) approach. Upper panel: Solid black line corresponds to total extinction, dotted black line to scattering, both for 7.5 µm-long Fe nanorods with cross-section 0.08 µm × 0.08 µm. Lower panel shows scattering asymmetry. Also shown in both panels are spectra for natural dust assuming a log-gaussian particle size distribution centered on 2.5 µm (48) (red dotted lines). In both panels, gray lines correspond to the results for a 9 µm-long Fe nanorod with cross-section 0.16 µm × 0.16 µm. As expected given its spectrum, the 7.5 µm-long nanorod gives ~2× less warming per nanorod in climate simulations. However, as it uses 5× less Fe, this design is more effective on a warming-per-unit-mass basis.
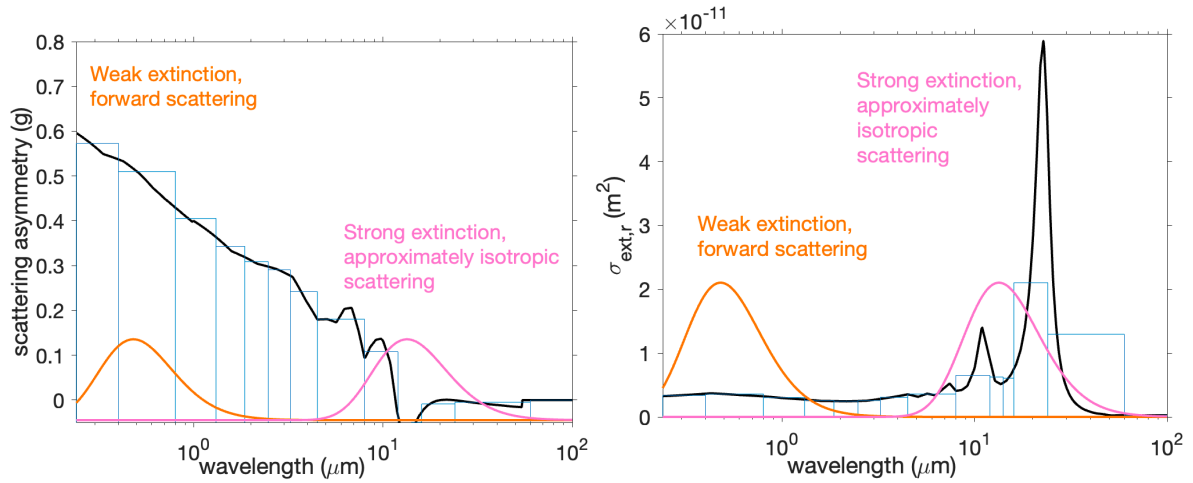
742

Fig. S9. Showing how the spectra are represented within the 3-D climate model. 9 µm-long, ~60:1 aspect ratio nanorod. 4.5 µm marks the separation between solar bins (Planck-weighted using the orange 6000 K blackbody curve, normalized W/m²/µm flux density), and thermal IR bins (Planck-weighted using the pink 215 K blackbody curve, normalized W/m²/µm flux density). The relative heights of the orange and pink Planck functions are to guide the eye only and have no physical significance.
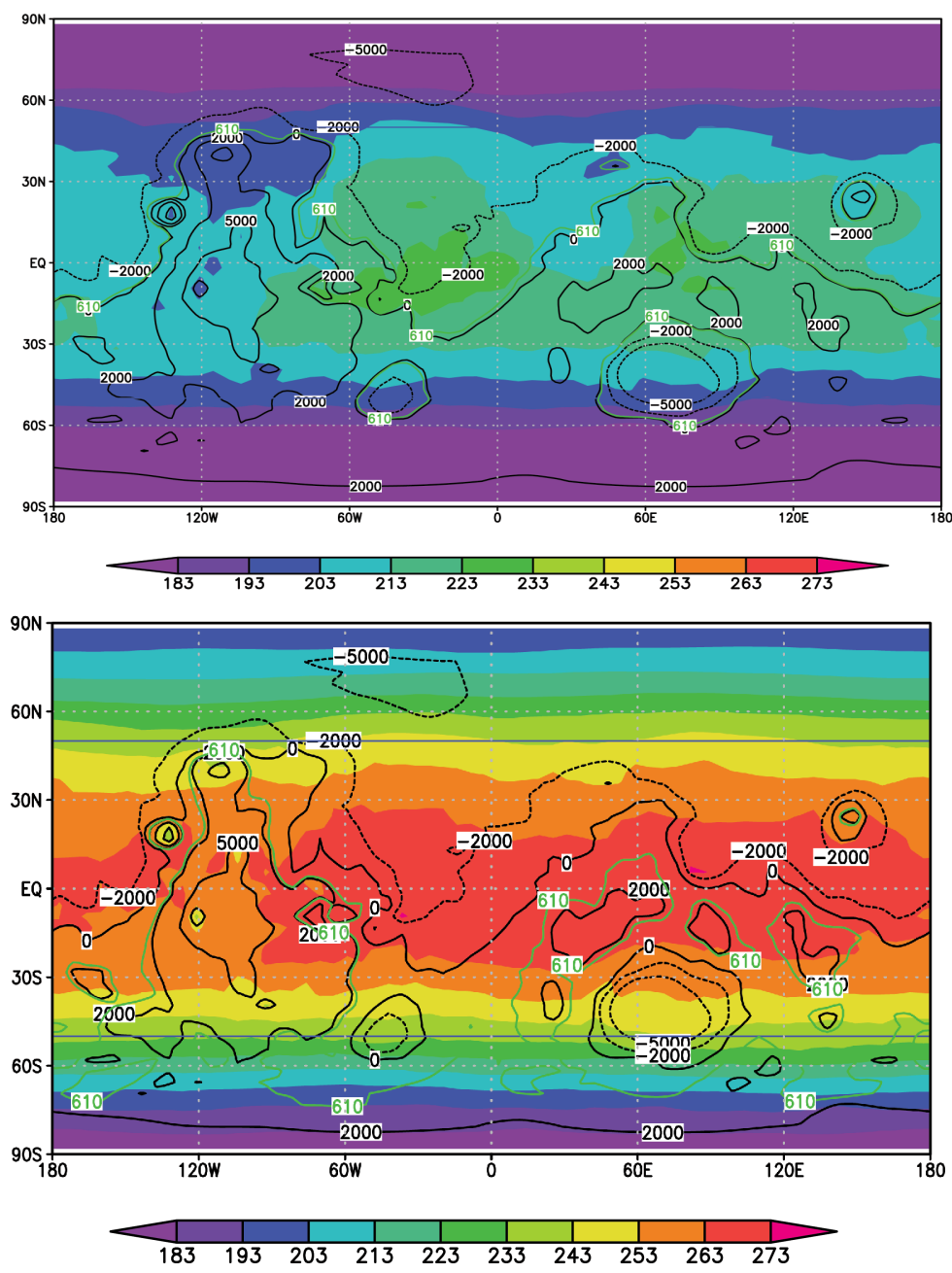
743

Fig. S10. Annual average temperatures (K) for (top) control simulation without nanorods (i.e., Fig. 2b), and (bottom) warmed case with ~160 mg/m^2 Al nanorods (i.e., Fig. 2a). Labeled black contours correspond to topographic elevation in m. Green contour corresponds to 610 Pa (~6 mbar) mean pressure level. Blue lines: approximate latitudinal (equatorward) extent of ice at <1 m depths.
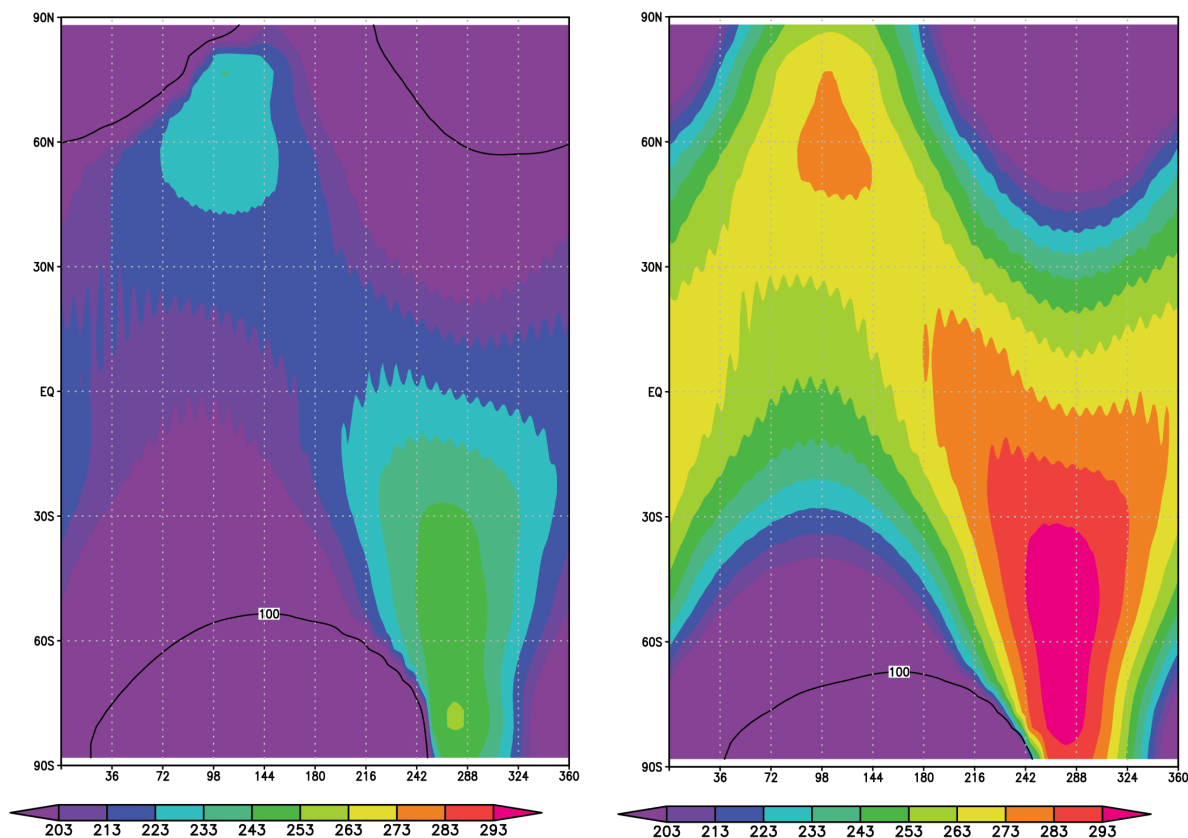
Fig. S11. Seasonal variation of diurnal-average surface temperature (K) for (left) control simulation without nanorods (i.e., Fig. 2b), and (right) warmed case with ~160 mg/m^2 nanorods (i.e., Fig. 2a), showing longitudinal average surface temperature. Each of the 10 increments on the x-axis, which are equally spaced in time, corresponds to 1/10 of a Mars year (69 Earth days). To make this figure, a 9-point smoother has been used (3 points in time, and 3 points in latitude) in order to damp oscillations associated with aliasing in the sampling of the day-night temperature cycle in the output. The black lines show the limit of substantial polar seasonal CO_2 ice.

746

33
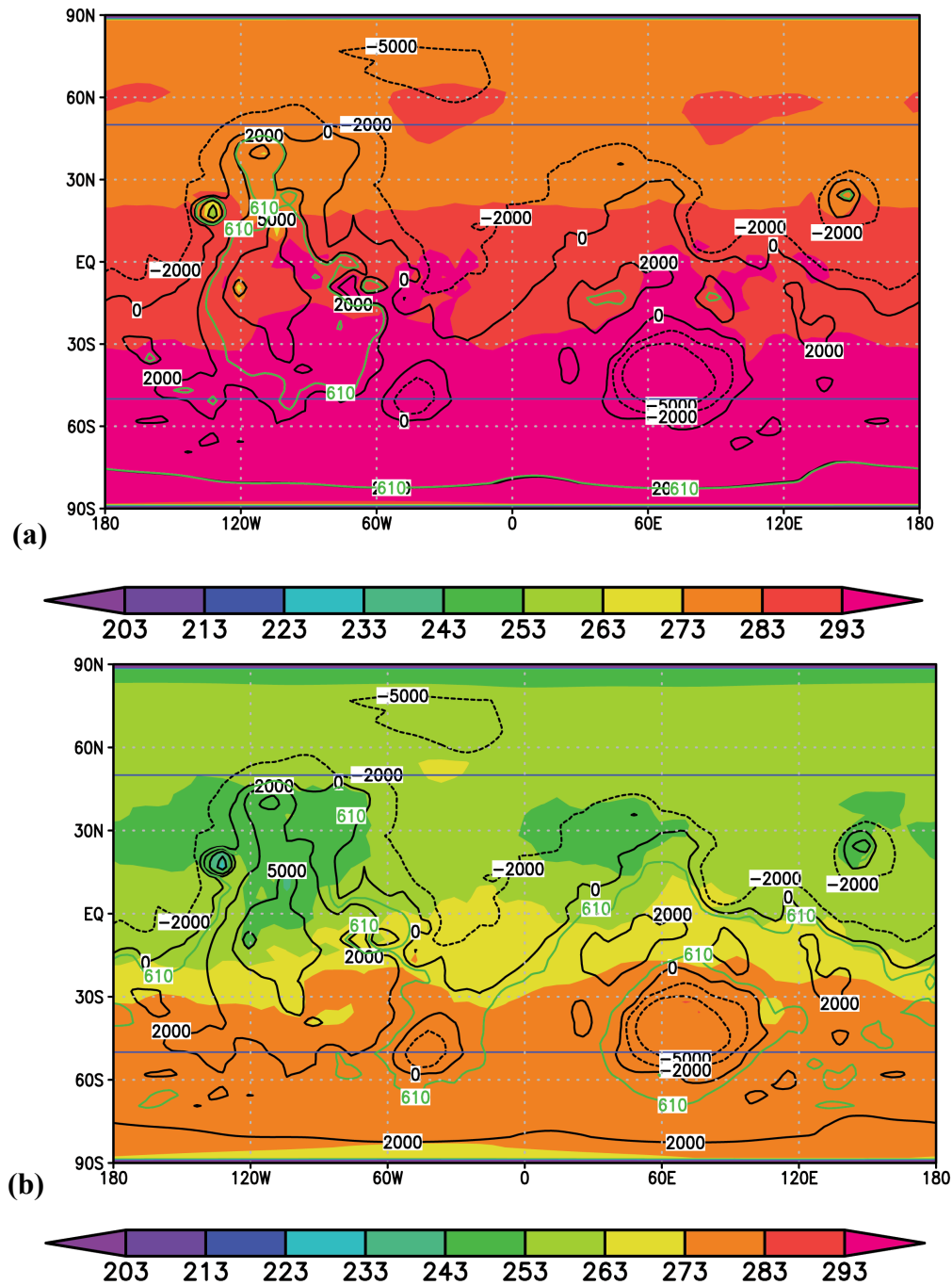
Fig. S12. Sensitivity tests showing how warm-season temperatures vary for different parameter choices. Baseline is Fe nanorod results shown in Fig. S19. Labeled black contours correspond to topographic elevation in m. Green contour corresponds to 610 Pa (~6 mbar) mean pressure level. Blue lines: approximate latitudinal (equatorward) extent of ice at <1 m depths. (a) More nanorods ($\tau_{Fe} = 1.5$): the average surface pressure exceeds 610 Pa (green contour) at all locations below +2 km elevation. (b) Fewer nanorods ($\tau_{Fe} = 0.375$).

34

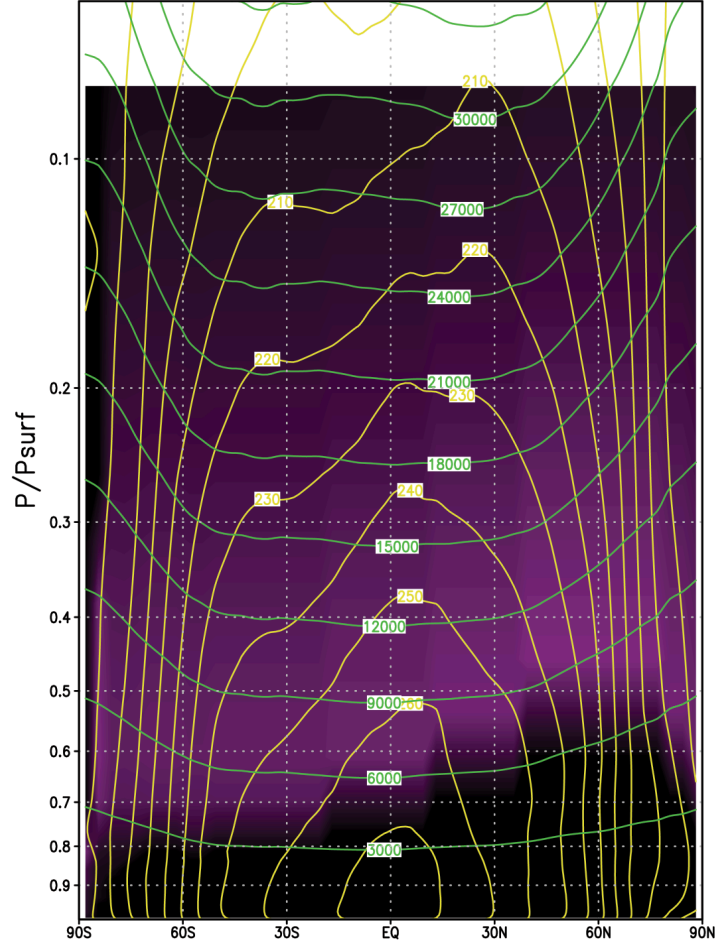**Fig. S13.** Cross section of steady (imposed) nanorod layer ($\tau_{Fe} = 0.75$, Fig. S19). The purple shading corresponds to the relative volume density of nanorods. The mixing ratio of nanorods within the purple layer is uniform, but there is more gas closer to the planet's surface so there are also more nanorods lower down. The tenuous part of the nanorod layer extending to high altitude is disproportionately important because of its strong contribution to the greenhouse effect. The Y-axis uses terrain-following η-coordinates ($\eta = P/P_{surf}$, where the model-top pressure has been subtracted from both pressures), and the cloud lines are tilted down and to the left because the southern hemisphere surface is topographically higher and thus closer to the fixed-pressure base of the nanorod layer. The yellow lines are contours of annual average atmospheric temperature. The green lines are contours of altitude in meters, which bow upwards at the poles where low temperatures compact the gas column.

748
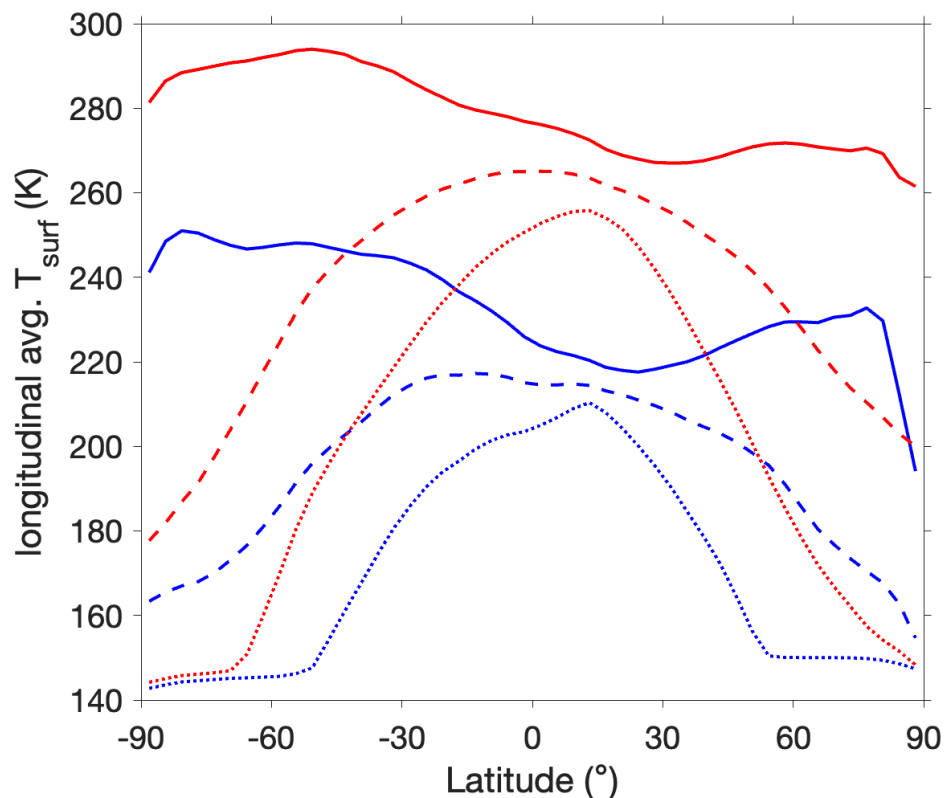
Fig. S14. Summary of the latitudinal and seasonal dependence of surface temperature for (red lines) the 3D model with-nanorods $\tau_{Fe} = 0.75$ case (Fig. S19a), and (blue lines) the 3D model without nanorods (Fig. S19b). Solid line corresponds to the average temperature during the warmest season (~70 day period) during the year, dotted line corresponds to the average temperature during the coldest season (~70 day period) of the year, and dashed line corresponds to the annual average. The flattening-out of the lines around 145 K corresponds to buffering at the frost point of CO_2.

749
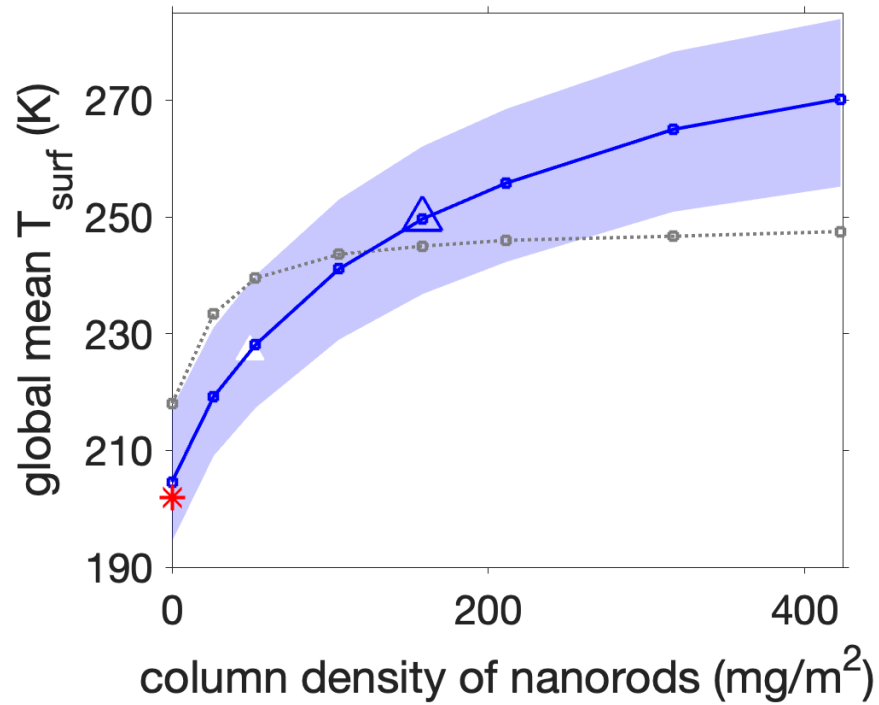
Fig. S15. As Fig 2c, but with a linear x-axis instead of a logarithmic x-axis. Dependence of planet-averaged surface warming on nanorod column mass. Blue triangle corresponds to Fig. 2a, the intersection of the blue line with the zero-nanorods axis corresponds to Fig. 2b, and white triangle marks onset of warm-season temperatures above the freezing point of water at 50°S. Blue corresponds to 3-D results. The blue envelope corresponds to the modeled seasonal range in global mean T_{surf}. Gray corresponds to 1-D results. The red asterisk corresponds to the observed modern Mars value.

Iron (Fe) **Aluminum (Al)**
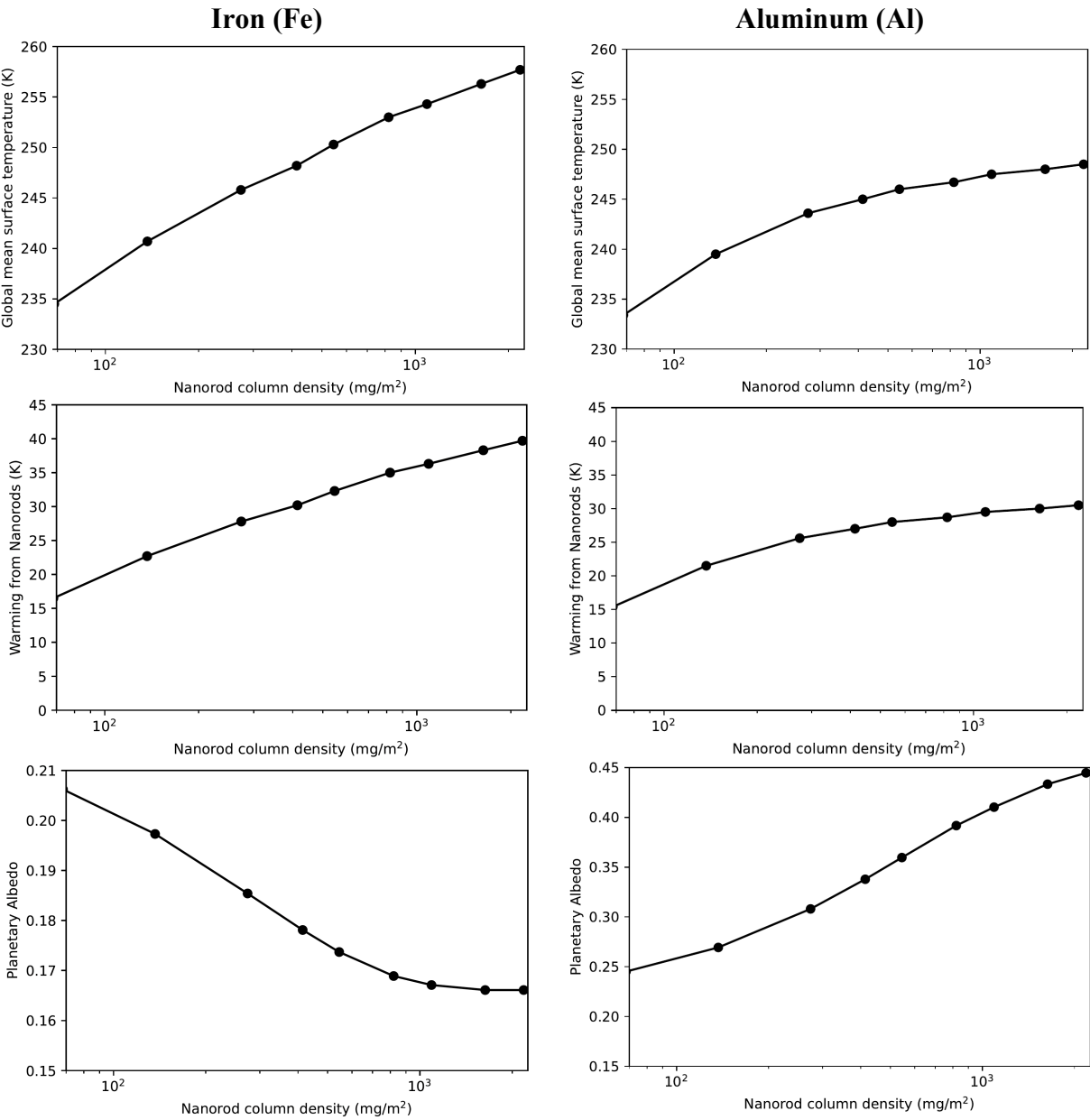
753 **Fig. S16.** Summary of 1-D climate model output as a function of nanorod column density. Left
754 column corresponds to Fe, right column corresponds to Al.

755
756

(a)
(b)
(c)
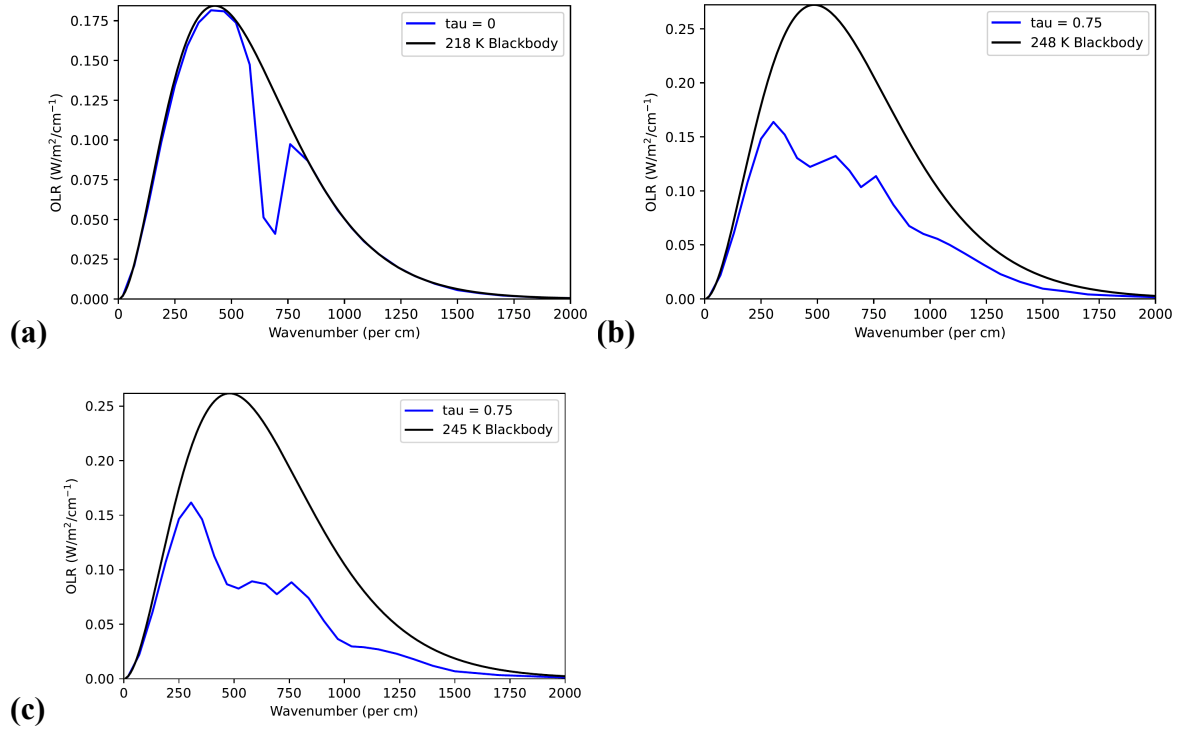
Fig. S17. Outgoing Longwave Radiation (OLR) from the 1D model. The integrated top-of-atmosphere OLR values are ~114.6, 96.6, and 120 W/m^2 for the no-nanorod, Al and Fe nanorod cases, respectively. **(a)** The no-nanorods case. Spectral windows are visible as peaks on either side of the CO_2 band which is at 600-800 per cm. **(b)** The nanorods case with $\tau_{Fe} = 0.75$. Absence of prominent peaks corresponds to closure of the spectral windows. **(c)** The nanorods case with $\tau_{Al} = 0.75$.
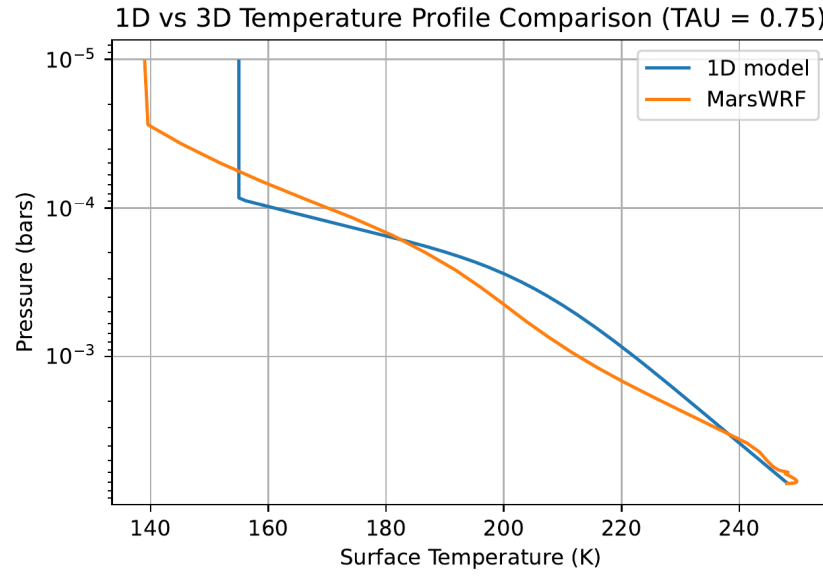
Fig. S18. 1D model vs. 3D (MarsWRF) model temperature profile comparison for τ_{Fe} = 0.75. The 3D result is the global and annual average. At this optical depth, surface temperature for both models is ∼ 250 K.

(a)

(b)

(c)
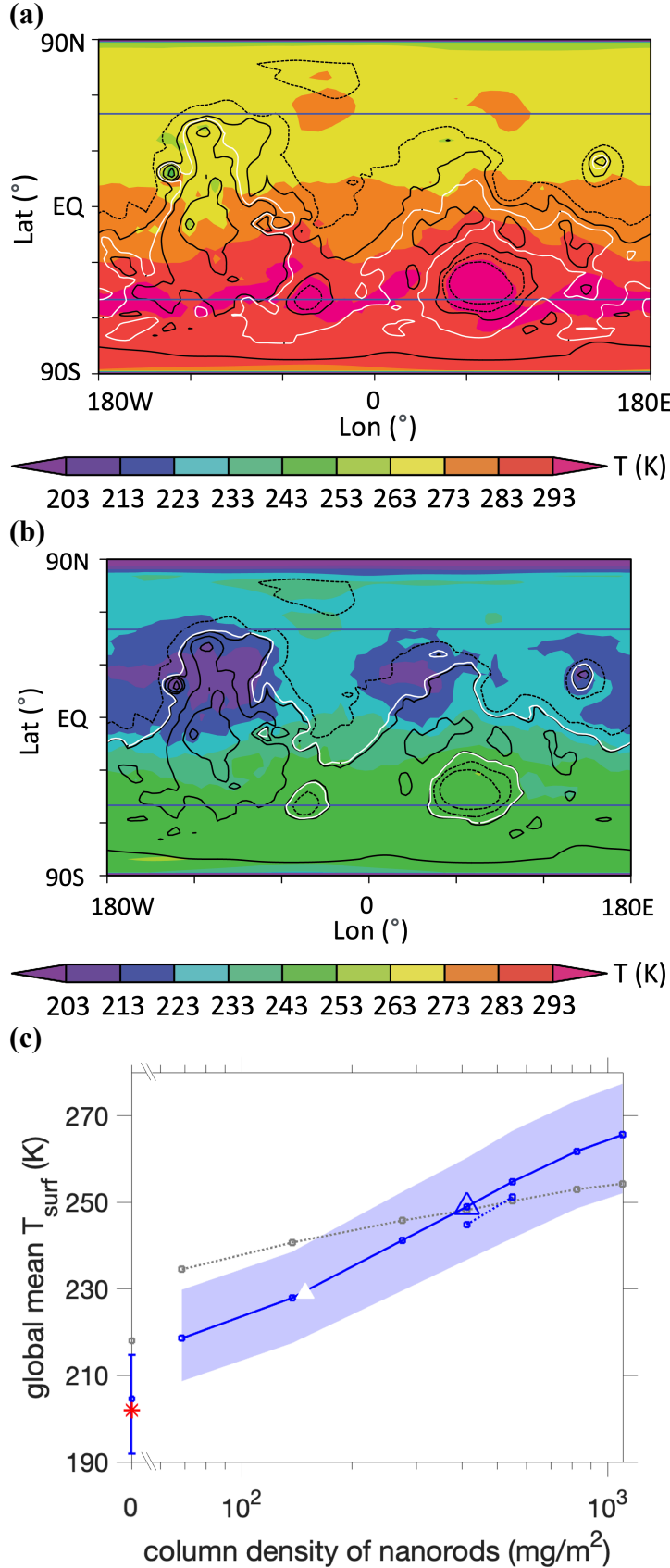
Fig. S19. As Fig. 2, but for 400 mg/m^2 loading of Fe nanorods instead of 160 mg/m^2 loading of Al nanorods. Warm-season temperatures (K) (color shading) on (a) Mars with addition of ~400 mg/m^2 of nanorods, (b) control case. This corresponds to the average surface temperature during the warmest 36° of solar longitude (~70 days) of the year. White contour corresponds to 610 Pa (~6 mbar) mean pressure level. Black contours correspond to topographic elevation in m (dashed: -5 km and –2 km, solid: 0 km, +2km, and +5 km). Blue lines: approximate latitudinal (equatorward) extent of ice at <1 m depths. Results do not include CO$_2$ outgassing from within polar ice, which would cause further warming. (c) Dependence of planet-averaged surface warming on nanorod column mass. Blue line corresponds to 3-D results, varying layer-top height between ~35 km (solid line) and ~28 km (dashed line). The blue envelope corresponds to the modeled seasonal range in global mean T_{surf}. Gray corresponds to 1-D results (see text for details). Blue triangle corresponds to panel (a), and white triangle marks onset of warm-season temperatures above the freezing point of water at 50°S. Symbols on y-axis are temperatures for the no-nanorod case, with the red asterisk corresponding to observed Mars value. More detail is shown in Figs. S10-S17.

Material	Iron (Fe)			Aluminum (Al)		
wavelength (×10^{-4} m)	absorption cross-section (×10^{-10} m^2)	scattering cross-section (×10^{-10} m^2)	asymmetry parameter (g)	absorption cross-section (×10^{-10} m^2)	scattering cross-section (×10^{-10} m^2)	asymmetry parameter (g)
0.0024	0.0131	0.0194	0.596	0.0114	0.0236	0.5204
0.0033	0.0133	0.0215	0.549	0.0053	0.0325	0.4205
0.0043	0.0138	0.0232	0.5327	0.0044	0.0351	0.4454
0.0052	0.0131	0.0226	0.505	0.0036	0.0298	0.4093
0.0061	0.0128	0.0214	0.4728	0.0034	0.0274	0.3687
0.007	0.0128	0.0205	0.4492	0.0037	0.0254	0.3548
0.008	0.0127	0.0196	0.4301	0.0045	0.0233	0.3536
0.0089	0.0125	0.0186	0.4131	0.0044	0.0220	0.3450
0.0098	0.0121	0.0177	0.3979	0.0028	0.0216	0.3350
0.01	0.0125	0.017	0.3997	0.0012	0.0221	0.3178
0.0158	0.0104	0.0148	0.3322	0.0011	0.0213	0.2824
0.0217	0.0098	0.0147	0.3041	0.0022	0.0274	0.2659
0.0275	0.0102	0.0152	0.2921	0.0032	0.0349	0.2400
0.0333	0.012	0.0168	0.2745	0.0048	0.0441	0.0693
0.0392	0.0127	0.0193	0.2218	0.0068	0.0562	0.0755
0.045	0.0163	0.0191	0.1798	0.0027	0.0303	0.1405
0.0508	0.0112	0.0203	0.1804	0.0043	0.0394	0.1514
0.0567	0.0152	0.0213	0.1732	0.0025	0.0377	0.1627
0.0625	0.012	0.0217	0.2035	0.0054	0.0532	0.1700
0.0683	0.0163	0.0271	0.206	0.0073	0.0588	0.0671
0.0742	0.0214	0.031	0.1553	0.0044	0.0443	0.0308
0.08	0.013	0.0278	0.0922	0.0046	0.0508	0.0664
0.0858	0.012	0.0302	0.119	0.0053	0.0650	0.0825
0.0917	0.0138	0.0347	0.1344	0.0101	0.0916	0.0818
0.0975	0.0225	0.0452	0.1368	0.0182	0.1456	0.0490
0.1	0.0247	0.0514	0.1327	0.0223	0.1579	0.0321
0.1092	0.0532	0.0886	0.0835	0.0130	0.0854	-0.0657
0.1184	0.0359	0.0619	-0.0233	0.0066	0.0549	-0.1176
0.1276	0.0165	0.0399	-0.0872	0.0057	0.0551	-0.1074
0.1367	0.0125	0.0387	-0.0822	0.0064	0.0630	-0.0808
0.1459	0.0126	0.0437	-0.057	0.0080	0.0768	-0.0579
0.1551	0.0145	0.0524	-0.0352	0.0107	0.0976	-0.0427
0.1643	0.0178	0.0644	-0.0205	0.0146	0.1274	-0.0337
0.1735	0.0234	0.0813	-0.0109	0.0215	0.1720	-0.0284
0.1827	0.032	0.1081	-0.0053	0.0327	0.2449	-0.0254
0.1918	0.0451	0.1489	-0.0018	0.0501	0.3503	-0.0240

0.201	0.067	0.2132	-0.0001	0.0700	0.4696	-0.0235
0.2102	0.0987	0.3056	0.0006	0.0818	0.5050	-0.0235
0.2194	0.1371	0.4119	0.0007	0.0707	0.4157	-0.0240
0.2286	0.1553	0.4378	0.0003	0.0501	0.2839	-0.0246
0.2378	0.1293	0.3514	-0.0004	0.0349	0.1829	-0.0252
0.2469	0.0886	0.2335	-0.0011	0.0246	0.1214	-0.0259
0.2561	0.0604	0.1484	-0.0019	0.0169	0.0840	-0.0268
0.2653	0.0428	0.099	-0.0028	0.0124	0.0599	-0.0276
0.2745	0.0304	0.0691	-0.0037	0.0101	0.0443	-0.0283
0.2837	0.0228	0.0495	-0.0044	0.0082	0.0340	-0.0289
0.2929	0.0186	0.0369	-0.0051	0.0065	0.0267	-0.0296
0.302	0.0154	0.0285	-0.0059	0.0053	0.0213	-0.0303
0.3112	0.0124	0.0224	-0.0066	0.0047	0.0172	-0.0309
0.3204	0.0103	0.0179	-0.0072	0.0042	0.0141	-0.0314
0.3296	0.0089	0.0145	-0.0077	0.0038	0.0117	-0.0318
0.3388	0.008	0.0119	-0.0081	0.0033	0.0098	-0.0321
0.348	0.007	0.0099	-0.0085	0.0028	0.0083	-0.0325
0.3571	0.0061	0.0084	-0.009	0.0026	0.0071	-0.0329
0.3663	0.0054	0.0071	-0.0095	0.0024	0.0061	-0.0332
0.3755	0.0049	0.0061	-0.01	0.0022	0.0053	-0.0335
0.3847	0.0045	0.0052	-0.0104	0.0020	0.0046	-0.0338
0.3939	0.0041	0.0046	-0.0108	0.0017	0.0040	-0.0340
0.4031	0.0036	0.004	-0.0112	0.0015	0.0036	-0.0342
0.4122	0.0032	0.0035	-0.0115	0.0014	0.0032	-0.0343
0.4214	0.0029	0.0031	-0.0119	0.0013	0.0028	-0.0345
0.4306	0.0027	0.0028	-0.0123	0.0014	0.0025	-0.0348
0.4398	0.0027	0.0025	-0.0127	0.0014	0.0023	-0.0350
0.449	0.0027	0.0022	-0.0132	0.0014	0.0021	-0.0352
0.4582	0.0026	0.002	-0.0136	0.0013	0.0019	-0.0353
0.4673	0.0024	0.0018	-0.0139	0.0011	0.0017	-0.0355
0.4765	0.0021	0.0017	-0.0143	0.0009	0.0016	-0.0356
0.4857	0.0018	0.0015	-0.0146	0.0007	0.0014	-0.0358
0.4949	0.0015	0.0014	-0.0149	0.0005	0.0013	-0.0359
0.5041	0.0013	0.0012	-0.0151	0.0003	0.0012	-0.0359
0.5133	0.0012	0.0011	-0.0153	0.0003	0.0011	-0.0360
0.5224	0.0012	0.001	-0.0155	0.0004	0.0010	-0.0361
0.5316	0.0013	0.0009	-0.0156	0.0006	0.0009	-0.0361
0.5408	0.0015	0.0009	-0.0158	0.0008	0.0008	-0.0362
0.55	0.0017	0.0008	-0.016	0.0010	0.0008	-0.0363

Supplementary Table 1: Orientation-averaged optical properties of nanorods as used in the climate simulations, corresponding to a 9 μm-long nanorod with cross-section (0.16×0.16) μm.

769

Optical depth (τ) at $\lambda = 0.67$ μm	Nanorod column mass (mg/m^2)	1-D temperature output, global mean (K)	3D temperature output		
			3-D global mean temperature (K)	50°N warm-season temperature (K)	50°S warm-season temperature (K)
0	0	218.0	204.6	228.8	250.3
0.125 (Al)	26.6	233.4	219.2	243.2	264.3
0.25 (Al)	53.2	239.5	228.1	253.0	274.4
0.5 (Al)	106.5	243.6	241.1	265.8	289.0
0.75 (Al)	161.2	245.0	249.7	274.3	298.2
1 (Al)	212.1	246.0	255.8	280.2	304.8
1.5 (Al)	319.4	246.7	265.0	287.6	312.3
2 (Al)	424.6	247.5	270.3	291.6	316.7
0.125 (Fe)	68.4	234.5	218.6	241.2	262.2
0.25 (Fe)	136.6	240.7	227.9	250.9	271.9
0.5 (Fe)	273.8	245.8	241.2	263.2	285.9
0.75 (Fe)	414.3	248.2	249.0	270.9	294.0
1 (Fe)	545.1	250.3	254.7	275.7	299.3
1.5 (Fe)	820.8	253.0	261.8	281.5	304.9
2 (Fe)	1091.1	254.3	265.6	285.0	307.1

770 **Supplementary Table 2.** Summary of climate model output. The nanorod column mass differs
771 between the Al and Fe cases by a factor of 2.57 (ratio of material densities, corrected for the 13%
772 greater extinction cross-section of Fe rods at 0.67 μm relative to Al rods).

773

Description	Optical depth (τ) at $\lambda = 0.67$ μm	3D temperature output		
		3-D global mean temperature (K)	50°N warm-season temperature (K)	50°S warm-season temperature (K)
Reference	*0.75*	*249.0*	*270.9*	*294.0*
Lower cloud top (~28 km vs. ~35 km)	0.75	244.8	270.6	289.5
Lower cloud top (~28 km vs. ~35 km)	1	251.2	275.6	297.1
2× atmospheric pressure (≈12 mbar)	0.75	252.7	269.9	290.1
Nanorods extend only from 45°S - 45°N	0.75	237.7	230.5	253.2
Nanorods only active from L_s = 180 – 360, passive at other seasons	0.75	224.9	229.2	293.3
5× greater output frequency	0.75	249.0	270.8	294.0
2× smaller numerical timestep	0.75	249.5	271.0	293.5
Thinner cloud (200 Pa base, 8 levels)	0.75	248.7	269.3	290.9
96×72 spatial grid in model (vs. default of 64×48)	0.75	250.5	271.1	292.9

774   **Supplementary Table 3.** Summary output for additional sensitivity tests using 3D model. All
775   were carried out using Fe nanorods.